



UNIVERSITY OF LEEDS

This is a repository copy of *P-T-X constraints on the Koru epithermal base-metal ( $\pm$ Au) deposit, Biga Peninsula, NW Turkey.*

White Rose Research Online URL for this paper:  
<http://eprints.whiterose.ac.uk/155997/>

Version: Accepted Version

---

**Article:**

Bozkaya, G, Bozkaya, O, Banks, DA [orcid.org/0000-0001-9118-5298](https://orcid.org/0000-0001-9118-5298) et al. (1 more author) (2020) P-T-X constraints on the Koru epithermal base-metal ( $\pm$ Au) deposit, Biga Peninsula, NW Turkey. *Ore Geology Reviews*, 119. 103349. ISSN 0169-1368

<https://doi.org/10.1016/j.oregeorev.2020.103349>

---

© 2020, Published by Elsevier B.V. This manuscript version is made available under the CC-BY-NC-ND 4.0 license <http://creativecommons.org/licenses/by-nc-nd/4.0/>.

**Reuse**

This article is distributed under the terms of the Creative Commons Attribution-NonCommercial-NoDerivs (CC BY-NC-ND) licence. This licence only allows you to download this work and share it with others as long as you credit the authors, but you can't change the article in any way or use it commercially. More information and the full terms of the licence here: <https://creativecommons.org/licenses/>

**Takedown**

If you consider content in White Rose Research Online to be in breach of UK law, please notify us by emailing [eprints@whiterose.ac.uk](mailto:eprints@whiterose.ac.uk) including the URL of the record and the reason for the withdrawal request.



[eprints@whiterose.ac.uk](mailto:eprints@whiterose.ac.uk)  
<https://eprints.whiterose.ac.uk/>

1  
2  
3  
4 P-T-X constraints on the Koru epithermal base-metal ( $\pm$ Au) deposit, Biga  
5  
6 Peninsula, NW Turkey  
7  
8

9 Gülcan Bozkaya <sup>a</sup>, Ömer Bozkaya <sup>a</sup>, David A. Banks <sup>b</sup>, Ahmet Gökçe <sup>c</sup>

10  
11  
12 <sup>a</sup>Department of Geological Engineering, Pamukkale University, 20070 Denizli, Turkey

13  
14 <sup>b</sup>School of Earth and Environment, University of Leeds, Woodhouse Lane, Leeds LS2 9JT, United Kingdom

15  
16 <sup>c</sup>Department of Geological Engineering, Cumhuriyet University, 58140 Sivas, Turkey  
17  
18  
19

20 **ABSTRACT**

21  
22 The Koru deposit is a typical intermediate sulfidation base-metal ( $\pm$  Au) example of volcanic-  
23 volcanoclastic hosted mineralization in the Biga Peninsula and north-western Turkey. Ore  
24 deposition was controlled by collisional and post-collisional tectonics related to the closure of  
25 the Tethys Ocean. Galena, baryte and quartz are main minerals, accompanied by minor  
26 amounts of sphalerite, pyrite, chalcopyrite, covellite and marcasite. The homogenization  
27 temperature of fluid inclusions indicates two distinct fluid pulses, one at a temperature  
28 commensurate with epithermal mineralization and boiling/near boiling conditions at c. 350 °C,  
29 the second approximately 150-200 °C lower. Salinity in both instances was from 11.0 to 0.2  
30 wt. % NaCl. The  $\delta$ D and  $\delta^{18}$ O values of water in equilibrium with early quartz and fluid  
31 inclusions, plot close to the magmatic water box indicating the source of the high temperature  
32 fluid was magmatic.  $\delta$ D and  $\delta^{18}$ O values from early and late baryte trend towards the  
33 meteoric water line (MWL), but this is not due to mixing with meteoric water and indicates  
34 equilibration with alteration assemblages. LA-ICP-MS analyses of fluid inclusions reveal high  
35 Cu-Zn-Pb concentrations in the fluids, despite their low salinity, transported as chloride  
36 complexes. The range of temperatures within the early quartz and sphalerite samples can be  
37  
38  
39  
40  
41  
42  
43  
44  
45  
46  
47  
48  
49  
50  
51  
52  
53  
54  
55  
56  
57  
58  
59

60 explained by pressure variations during vein and fracture opening from near lithostatic to  
61 hydrostatic pressure.  
62  
63  
64  
65

66 **Keywords:** Epithermal, Fluid Inclusion, Koru, Turkey, Base-metals, Gold  
67  
68

## 69 **1. Introduction**

70

71  
72 The Turkish segment of the Tethyan Eurasian Metallogenic Belt, which extends from  
73 Western Europe through Anatolia to Iran (Fig. 1a, Janković, 1986; Yigit, 2012), is currently  
74 being intensively prospected and contains an increasing number of active mines with Turkey  
75 becoming a world-class gold-producing country over the last 20 years. The majority of the  
76 deposits, in northwest Turkey, are low to intermediate sulfidation (LS-IS) Au + Ag deposits,  
77 often with gold as the main resource or in lesser amounts associated with Pb-Zn  
78 mineralization. A number of the epithermal Au-Ag (high and low sulfidation/HS-LS),  
79 porphyry Au-Cu-Mo and base metal skarn deposits and mineralizations are associated with  
80 Tertiary calc-alkaline magmatism in Western Anatolia and the Biga Peninsula (Fig. 1b and  
81 Table 1). The epithermal deposits in the Biga Peninsula have the same geological  
82 characteristics as other deposits of this style around the globe. Fluid inclusion studies (Unal et  
83 al, 2013; Yilmaz et al., 2010, 2013; Orgün et al., 2005; Oyman et al., 2003; Bozkaya and  
84 Banks, 2105a,b; Bozkaya et al., 2014, 2016) show that the mineralizing fluids were similar in  
85 the Turkish deposits and comparable with deposits of similar style and classification  
86 worldwide. Low salinity fluids pre-dominate at deposits where Au is the main resource,  
87 however at deposits where base-metal sulfides are the main resource, with lesser amounts of  
88 Au and Ag, higher salinity fluids and the low salinity fluids are present.  
89  
90  
91  
92  
93  
94  
95  
96  
97  
98  
99  
100  
101  
102  
103  
104  
105  
106  
107

108 The Koru deposit can be considered an IS epithermal deposit, hosted by volcanic-  
109 volcanoclastic units related to the collisional and post-collisional tectonic regime in Biga  
110 Peninsula (Yigit, 2012). There are many studies on the genesis of ore deposition and sources  
111  
112  
113  
114

119  
120  
121 of fluids in the Biga Peninsula, such as those listed in Table 1. Frequently, a fluid mixing  
122 model is inferred for mineralization due to the wide range of salinities and homogenization  
123 temperatures of fluid inclusions that are present (Oyman et al., 2003; **Orgün** et al. 2005;  
124 Yilmaz et al. 2010, 2013, Unal et al., 2013). In this study we present an alternative  
125 interpretation to meteoric fluid mixing with magmatic fluids that was previously been  
126 proposed. Based on the petrography, paragenesis of fluid inclusions, microthermometry and  
127 laser ablation inductively coupled plasma-mass spectrometry (LA-ICP-MS) analyses of fluid  
128 inclusions, combined with oxygen and hydrogen isotope analyses from quartz, baryte  
129 (Bozkaya and Gökçe, 2009; Bozkaya et al., 2016) sulfur isotope data from galena, sphalerite  
130 and baryte and propose that all the salinity fluids had a dominantly magmatic origin. A better  
131 understanding of the fluid composition and the key physical processes, which led to  
132 mineralization in the Koru deposit, can be applied to understand why, in the Biga peninsula,  
133 some **deposits are dominantly gold deposits and some are dominantly base-metals with minor**  
134 **amounts of gold.**  
135  
136  
137  
138  
139  
140  
141  
142  
143  
144  
145  
146  
147  
148  
149  
150  
151

## 152 **2. Geology and Mineralization**

### 153 *2.1. Regional Geological Setting*

154  
155  
156 The Biga Peninsula which is part of the Tethyan Eurasian Metallogenic Belt  
157 represents the westernmost extension of the Sakarya Zone of Pontides, at the intersection of  
158 Gondwana (African and Arabian plates) and Laurasia (Eurasian plate) (Jankovic, 1986; Okay  
159 et al., 1990; 1991; **Yigit**, 2012) (Fig. 1a). This area therefore, has a complicated geologic and  
160 tectonic history due to the collision of different continental fragments. The peninsula can be  
161 tectonically sub-divided into three zones going from the northwest to southeast. These are the  
162 Ezine zone (Permian metasedimentary and Permo-Triassic ophiolitic rocks), the Ayvacık-  
163 Karabiga zone (eclogite-bearing ophiolitic mélangé and Late Triassic limestone blocks) and  
164  
165  
166  
167  
168  
169  
170  
171  
172  
173  
174  
175  
176  
177

178  
179  
180 the Sakarya zone (Permian metamorphic rocks of the Kazdağ Group and Permo-Triassic  
181  
182 metasedimentary and metamagmatic rocks of the Karakaya Complex) (Fig. 1b). Cenozoic  
183  
184 volcanic and plutonic rocks cover extensive areas and dominate the geology of the Biga  
185  
186 Peninsula. The Late Cretaceous-Tertiary period has been divided into four different sub-  
187  
188 periods: (1) the Late Cretaceous-Early Eocene (turbiditic sandstones and limestones), (2)  
189  
190 Middle Eocene-Oligocene (andesitic lavas and tuffs, granite, granodiorite and limestones), (3)  
191  
192 Miocene (granodiorite, rhyolitic and rhyodacitic pyroclastics, andesitic and dacitic lavas, and  
193  
194 turbiditic clastics) and (4) Plio-Quaternary (fluvial sediments and lacustrine carbonates).  
195  
196 Regional uplift occurred at the end of the Oligocene resulting in the Eocene-Oligocene  
197  
198 sequence being deeply eroded. This was followed by extensive late Oligocene to middle  
199  
200 Miocene calc-alkaline magmatism. Granodioritic plutons and andesitic-dacitic volcanic rocks  
201  
202 developed during the Eocene with Oligocene granite, granodiorite, syenite and early Miocene  
203  
204 rhyolite, dacite and calc-alkaline andesites. In the Thrace basin and the Biga Peninsula, Na-  
205  
206 alkali basalts were emplaced during the late Miocene. The sedimentary, volcano-sedimentary,  
207  
208 volcanic and associated plutonic rocks in the Biga Peninsula are all related to the transition  
209  
210 from a collisional to an extensional tectonic regime during the period of Cenozoic calc-  
211  
212 alkaline magmatism from 52 to 18 Ma (Yigit, 2006; 2012) (Fig. 1b).  
213  
214  
215  
216  
217

## 2.2. Local Geology and Mineralization

220 The Koru mine is located in the northwest part of the Biga Peninsula, 50 km from  
221  
222 Çanakkale (Fig. 2) and had a total reserve of 0.5 Mt at 8 % Pb, 2 % Zn, 300 g/t Ag (Bozkaya,  
223  
224 2001). Mineralization is in veins, stockworks and breccias controlled by a NW trending fault  
225  
226 system. Several Pb-Zn deposits in the Koru district are located within a triangular area defined  
227  
228 by the villages of Koru, Eskikişla and Karaömerler (Fig. 2) hosted by Oligocene pyroclastic  
229  
230 rocks. These are, from NW to SE, Eskikişla, Tahtalıkuyu, İkinci Viraj, Bakır Kuyusu, Derin  
231  
232

237  
238  
239 Dere, **Kuyutaşı Tepe**, Sarioluk and Tesbihdere. The Tahtalıkuyu and **Eskikişla** deposits were  
240  
241 the most active mining areas of the Kuru district, therefore, most of the samples in this study  
242  
243 were collected from these when mining was active (Fig. 2). All the deposits were exploited by  
244  
245 the **Çanakkale** Mining Company, but none are currently active.  
246  
247

248 The volcanogenic rocks hosting Pb-Zn deposits consist of agglomerate, lapillistone and  
249  
250 tuff with andesite intercalations in the lower parts of the ore bearing sequence, silicified  
251  
252 rhyolitic breccias in the middle parts and silicified rhyolitic tuffs in the upper parts (Fig. 2).  
253  
254 All rock types were affected by hydrothermal alteration, to a variable degree, which produced  
255  
256 quartz + kaolinite and/or illite and/or illite-smectite with small amounts of alunite (Bozkaya et  
257  
258 al., 2016). The green color of pyroclastic rocks in the lower parts is mostly related to  
259  
260 zeolitization and chloritization resulting from interaction between volcanic glass and seawater  
261  
262 (Bozkaya et al., 2007). Silicification increases in the middle and upper parts of the ore bearing  
263  
264 sequence, with the main components of the pyroclastic breccias and tuffs formed from  
265  
266 intensely silicified rocks (Fig. 2). Tuffs from the upper parts of ore bearing sequence are  
267  
268 generally lithic ash tuffs with a large amount of volcanic rock fragments with an argillized  
269  
270 and silicified volcanic matrix (Fig. 3a). Silicified vitric ash tuffs contain coarse-grained quartz  
271  
272 replacing feldspars with devitrification of the volcanic glass (Fig. 3b,c). Stockwork type  
273  
274 veinlets become dominant in the silicified-tuffs and in the upper parts of the succession,  
275  
276 whereas massive and/or layered veins oriented WNW-ESE, are most common in the lower  
277  
278 parts (Fig. 2). In the **Tahtalıkuyu** and **Eskikişla** sectors, the vein-type mineralization in deeper  
279  
280 parts and stockwork-type mineralization in upper parts show depositional styles that are  
281  
282 comparable with volcanogenic massive sulfide deposits. However, the mineralized fault and  
283  
284 stockwork zone cuts the overlying tuffs and in the stockwork-type zones mineralization fills  
285  
286 spaces between the agglomerates. **In addition** the lack of stratiform mineralized lenses and  
287  
288 layers **indicates that** the Kuru base metal mineralization is epigenetic, occurring after the  
289  
290  
291  
292  
293  
294  
295

296  
297  
298 deposition of the volcano-sedimentary rocks (Bozkaya, 2001; Bozkaya and Gökçe, 2001,  
299  
300 2002, 2009).

301  
302 In the mineralized veins, sphalerite, galena, pyrite, chalcopyrite, quartz, baryte and  
303  
304 calcite are the main minerals, accompanied by small amounts of tennantite-tetrahedrite,  
305  
306 marcasite, covellite, bornite and small amounts of native gold (Fig. 4). Galena and sphalerite  
307  
308 generally exhibit anhedral or rarely subhedral crystals. Microscopic studies (Fig. 3d-g) show  
309  
310 these minerals were formed in at least two episodes. As seen in Fig. 3d, early-stage sphalerite  
311  
312 crystals are cracked and disaggregated by later deformation with a brecciated texture where  
313  
314 the fractures were filled by late-stage galena. In another example, the early-stage galena was  
315  
316 replaced by later sphalerite and chalcopyrite (Fig. 3e). Chalcopyrite is generally the last  
317  
318 sulfide to precipitate and almost all contains inclusions of galena and sphalerite (Fig. 3f).  
319  
320 Galena also contains rod-like tennantite-tetrahedrite crystals as late-stage sulfide segregations  
321  
322 (Fig. 3g). Baryte and lesser quartz are the main gangue minerals in the deposit, with their  
323  
324 crystal sizes increasing with depth. Baryte forms lath-shape euhedral crystals accompanied by  
325  
326 quartz and carbonate minerals. Relatively coarse-grained baryte crystals sometimes exhibit a  
327  
328 comb texture and are observed to cut the earlier anhedral quartz and calcite crystals (Fig. 3h,i).  
329  
330 The two generations of baryte can be distinguished as the early, small irregular crystals are  
331  
332 cut by later, large elongate crystals. The large elongate baryte crystals are also observed to cut  
333  
334 the anhedral quartz and calcite (Fig. 5).  
335  
336  
337  
338  
339

### 340 341 **3. Analytical Methods**

#### 342 343 *3.1. Microthermometry*

344  
345 Microthermometry of the fluid inclusions was carried out using a Linkam THMS 600  
346  
347 heating-cooling stage at the Fluid Inclusion Laboratory of the Department of Geological  
348  
349 Engineering Pamukkale University (Turkey). The temperature of phase changes for eutectic  
350

355 melting ( $T_e$ ), ice melting ( $T_{m_{ice}}$ ) and homogenization ( $T_h$ ) were recorded. Phase transitions  
356  
357 below 0 °C are accurate to within  $\pm 0.2$  °C based on calibration with pure CO<sub>2</sub> and H<sub>2</sub>O  
358  
359 standards, with a similar level of precision. Above 0 °C accuracy was  $\pm 3$  °C based on the  
360  
361 melting point of pure solids and precision was  $\pm 1$  °C. The ice-melting temperatures were  
362  
363 converted to salinities using the equation of Bodnar (1993), and assuming the fluid  
364  
365 composition is represented by the H<sub>2</sub>O - NaCl system.  
366  
367  
368  
369  
370  
371

### 372 *3.2. LA-ICP-MS*

373  
374 The chemical analysis of individual fluid inclusions, or fluid inclusion assemblages,  
375  
376 was made by LA-ICP-MS using an Agilent 7500c mass spectrometer, combined with a  
377  
378 Geolas ablation system at Leeds University (UK). This system uses a Compex 103 ArF  
379  
380 excimer laser producing a wavelength of 193 nm with an energy density between 10 – 15 J  
381  
382 cm<sup>-2</sup> at the sample surface. The operating frequency of the laser was typically 5 Hz with spot  
383  
384 sizes of 25 µm, occasionally 50 µm, and the main criteria being that the size was greater than  
385  
386 that of the inclusions. The ablated material was transported from the ablation cell to an  
387  
388 Agilent 7500c ICP-MS using 99.9999 % He flowing at 2 ml min<sup>-1</sup> into a cyclone mixer  
389  
390 where it was combined with the Ar carrier gas flowing at 1.02 ml min<sup>-1</sup>. The mixer prolongs  
391  
392 the signal from the ablated inclusions and improves precision by increasing the number of  
393  
394 cycles of the mass spectrometer through the selected elements and therefore the number of  
395  
396 determinations of each element/Na ratio that are made. The instrument was operated in  
397  
398 reaction cell mode using 2.5 ml min<sup>-1</sup> 99.9999 % H<sub>2</sub> to remove interferences on the main <sup>40</sup>Ca  
399  
400 isotope by <sup>40</sup>Ar and the main <sup>56</sup>Fe isotope by <sup>56</sup>Ar. Element/Na intensity ratios from the mass  
401  
402 spectrometer were converted to weight/weight ratios using the NIST glass SRM-610 and the  
403  
404 soda lime SRM-1412 as calibration standards. SRM 1412 is used specifically for the  
405  
406 calibration of K/Na as it has a K/Na ratio of 0.988 compared to the K/Na ratio for NIST 610  
407  
408  
409  
410  
411  
412  
413

414  
415  
416 of 0.0047 which is very different to the values measured from the fluid inclusions. The NIST  
417  
418 SRM-610 standard was used to check for instrumental drift, which was found to be  
419  
420 insignificant over each day's analysis. Integration of the standard and sample signals used the  
421  
422 SILLS software package (Guillong et al., 2008). Full details of the analytical protocols and  
423  
424 calibration of the instrument were presented in Allan et al. (2005).  
425  
426  
427  
428

### 429 *3.3. Hydrogen and oxygen isotopes*

431  
432 The hydrogen and oxygen isotope data of quartz and illite in Koru deposit were  
433  
434 reported in Bozkaya et al. (2016). Fluid inclusions from baryte samples were analysed for  $\delta D$   
435  
436 (fluid inclusions) and  $\delta^{18}O$ . O-isotope analyses were performed using an automatic  $CO_2$  laser-  
437  
438  $BrF_5$  fluorination system with a Micromass Optima mass spectrometer in the Stable Isotopes  
439  
440 Laboratories, Royal Holloway University of London (UK). Approximately 1.7 mg of baryte  
441  
442 was analysed to obtain  $\delta^{18}O$  values that are reported relative to the Vienna Ocean Water  
443  
444 Standard (V-SMOW). The analytical precision on standard and sample duplicates was  $\pm$   
445  
446 0.1 ‰. Hydrogen isotope analysis was carried out on fluid inclusions from baryte separates by  
447  
448 thermal decrepitation. The extracted water vapor was converted to hydrogen gas, and the  $\delta D$   
449  
450 of each sample was determined. H-isotope analyses were performed with a Micromass Iso  
451  
452 Prime mass spectrometer in the Stable Isotope Laboratories, University of Nevada (USA) and  
453  
454 are reported as  $\delta D$  ‰ notations versus V-SMOW) with analytical precisions of  $\pm$  1.0 ‰.  
455  
456  
457  
458  
459

## 460 **4. Results**

### 461 462 *4.1. Fluid Inclusion Petrography*

463  
464 Fluid inclusions are abundant in quartz, sphalerite and baryte, and those measured  
465  
466 were predominantly primary in origin, occurring in growth bands or in fluid inclusion arrays  
467  
468

473  
474  
475 that were related to the paragenesis of the host minerals. Two types of quartz have been  
476 identified: the more prevalent is euhedral quartz (Qz-1) which has numerous euhedral  
477 overgrowths that are often delineated by bands of primary fluid inclusions oriented  
478 perpendicular to the crystal faces, or contain random individual primary fluid inclusions  
479 especially in the inner quartz core (Fig. 5, 6a). Within individual growth bands, the fluid  
480 inclusions have variable Liquid (L)/Vapor (V) ratios and often contain V-rich fluid inclusions  
481 (Fig. 6b). The primary fluid inclusions in quartz were also found in clusters and have a  
482 feather-like structure resulting from their trapping on different quartz faces. These are features  
483 commonly observed in epithermal environments (Dong et al., 1995; Moncada et al., 2017)  
484 and also in other deposits in the Biga Peninsula (Bozkaya et al., 2014; Bozkaya and Banks,  
485 2015a,b). There are examples of co-existing V-rich, L-V fluid inclusions and fluid inclusions  
486 containing semi-prismatic solids, probably trapped during boiling (Fig. 6 e,f). These prismatic  
487 crystals are birefringent in crossed polars (possibly illite) and are common in fluid inclusions  
488 however, they are very uncommon in the quartz matrix (Moncada and Bodnar, 2012;  
489 Moncada et al., 2012). The second type of quartz was observed in places to replace the earlier  
490 euhedral quartz, or more commonly to abut these crystals. These smaller anhedral crystals are  
491 cleaner in appearance with fewer fluid inclusions. The fluid inclusions are mainly randomly  
492 dispersed, but are also present in fluid inclusion arrays (FIA's) that extend to the crystal edge  
493 and do not penetrate into the adjacent crystals. All the fluid inclusions are L-V with larger and  
494 more consistent L/V ratios than fluid inclusions observed in the first generation of quartz.

495  
496  
497 Two generations of sphalerite were identified by their texture, but were most easily  
498 distinguished by the darker colour of the early sphalerite and the lighter colour of the later  
499 sphalerite. The fluid inclusions in the first generation are similar those observed in the  
500 euhedral quartz with random L-V fluid inclusions and many that are V-rich in close proximity

532  
533  
534 to each other (Fig. 6c) **which is indicative** of boiling. In addition, there are secondary trails of  
535  
536 smaller more numerous L-V fluid inclusions cutting the early sphalerite. The second  
537  
538 generation of lighter sphalerite also contains primary fluid inclusions of a similar size and  
539  
540 with the same L/V ratios as the secondary **fluid** inclusions in the dark early sphalerite.  
541  
542

543  
544 There are two generations of baryte, both of **which cut** the second generation of quartz  
545  
546 and are **the final phases** to precipitate (Fig. 6d). The fluid inclusions in baryte are mainly L-  
547  
548 only but there are some L-V fluid inclusions with small bubbles (Fig. 6e, f). The second  
549  
550 generation of baryte contains a large number of small primary fluid inclusions that are **L-only**  
551  
552 **and delineate** crystallographic growth zones. **This baryte also contains** pseudosecondary and  
553  
554 secondary fluid inclusions that are L-only (Fig. 6g). There are also a small number of **L-V**  
555  
556 **fluid inclusions that occur** in the same arrays as L-only fluid inclusions (Fig. 6h). As fluid  
557  
558 inclusions in baryte frequently stretch or leak (**Ulrich and Bodnar, 1988**) it is highly likely,  
559  
560 given the association with L-only arrays, **that the vapor phase may** have been artificially  
561  
562 produced. Baryte is also observed to replace the **earlier** euhedral quartz crystals, which then  
563  
564 contain **the same** secondary trails of L-only **fluid** inclusions **as in the baryte** (Fig. 6i,j).  
565  
566

#### 567 568 *4.2. Microthermometry*

569  
570 A summary of the microthermometry data for fluid inclusions in quartz, sphalerite and  
571  
572 baryte are presented in Table 2. In quartz and sphalerite the eutectic melting **temperature (Te)**  
573  
574 was observed between -40°C and -50°C. The majority of **fluid** inclusions homogenize to  
575  
576 liquid ( $T_{h_{liq}}$ ) and comprise the bulk of the measurements. **These data** are given as the average,  
577  
578 minimum and maximum-recorded homogenization temperatures (**Th**), along with a smaller  
579  
580 number of **VL fluid** inclusions **that homogenized** to a **vapor phase**. These values are shown  
581  
582 graphically (Fig. 7) as a box and whisker **plot where** the shaded box represents the 25<sup>th</sup> to 75<sup>th</sup>  
583  
584 percentile range, the horizontal lines are the 5<sup>th</sup> and 95<sup>th</sup> percentile values and individual  
585  
586  
587  
588  
589  
590

591  
592  
593 points are outliers. The mean and median values (black and white horizontal lines in the  
594 shaded box) are in most cases identical and the data is **therefore** normally distributed. This  
595 approach allows a clearer visual appreciation of the data.  
596  
597  
598

600 The homogenization temperature data for the fluid inclusions in quartz, sphalerite and  
601 barite are given in Fig. 8. In Qz-1  $T_{h_{liq}}$  values are between 249 °C and 354 °C, in Qz-2  
602 between 166 °C and 251 °C and  $T_{h_{vap}}$  homogenization for **vapor-rich** inclusions associated  
603 with Qz-1 are between 315 °C and 354 °C (Figs. 7, 8). In Sp-1  $T_{h_{liq}}$  values are between 248  
604 °C and 341 °C, although there were some V-rich **fluid** inclusions where homogenization could  
605 not be observed due to the darkness of the sphalerite. In Sph-2  $T_{h_{liq}}$  was between 134 °C and  
606 228 °C.  $T_{h_{liq}}$  values for fluid inclusions in Brt-1 were between 70 °C and 217 °C, but the large  
607 range and the petrography of the L-V fluid inclusions makes us treat these values with caution.  
608 In Brt-2 the vast majority of fluid inclusions are L-only and  $T_h$  could not be measured. The  
609  $T_{m_{ice}}$  values for L-V fluid inclusions in Qz-1 are between -0.9 °C and -5.1 °C (1.6 to 8 equiv  
610 wt.% NaCl), Qz-2 between -0.6 °C and -5.6 °C (1.1 to 8.7 equiv. wt.% NaCl) but could not be  
611 observed in V-rich fluid inclusions (Fig. 9). In Sp-1  $T_{m_{ice}}$  are between -1.8 °C and -5.5 °C  
612 (3.1 to 8.7 equiv. wt.% NaCl) and in Sph-2 between -0.1 °C and -7.5 °C (0.2 to 11.1 equiv.  
613 wt.% NaCl). In Brt-1  $T_{m_{ice}}$  are between -0.3 °C and -3.4 °C (0.5 to 5.5 equiv. wt.% NaCl) and  
614 where fluid inclusions in Brt-2 had a **vapor** phase (although they occur amongst fluid  
615 inclusions which only had liquid and the **vapor** was likely an artefact) the salinity of the fluid  
616 inclusions **covered a** similar range. The salinities **of the fluid** inclusions in the different  
617 minerals essentially covers the same range, however the highest salinities are **recorded** in  
618 sphalerite hosted inclusions.  
619  
620  
621  
622  
623  
624  
625  
626  
627  
628  
629  
630  
631  
632  
633  
634  
635  
636  
637  
638  
639  
640  
641  
642  
643  
644  
645  
646  
647  
648  
649

#### 4.3. LA-ICP-MS

The element/Na weight ratios for fluid inclusions, ablated in quartz, baryte and sphalerite, are presented in Fig. 10 and Table 3 together with the standard deviation and where appropriate the concentration of the elements calculated using salinity from microthermometry measurements. Table 3 contains two columns for K/Na ratios ( $K^*$  and K) as the data have been separated into high ( $K^*/Na$ ) and low (K/Na) ratios that are statistically different. The  $K^*/Na$  ratios are from inclusions where we have observed or suspect the presence of illite (Fig. 6e) in the inclusions which would increase the ablation signal for K adding to the K signal from the fluid phase. In quartz, the primary L-V or V-rich fluid inclusions, where we do not see any solid phase in the fluid inclusion, have lower K/Na ratios. However, there appears not to be a significant difference in the ratios of other elements/Na that were determined, between fluid inclusions that contain a solid and those that do not. The data are shown in Fig. 10 which illustrates the similarities of the trace element ratios.

#### 4.4. Hydrogen and Oxygen Isotopes

The measured  $\delta^{18}O$  values for baryte (Brt-1) and quartz crystals (Qz-1), the calculated  $\delta^{18}O$  values for fluid inclusion water in equilibrium with baryte and quartz, together with  $\delta D$  values for the fluid inclusions are given in Fig. 11 and Table 4. Baryte crystals have measured  $\delta^{18}O$  values ranging from +7.4 to +14.5 ‰, and 14.2 ‰ for quartz. The calculated  $\delta^{18}O$  values for water in equilibrium with baryte and quartz was determined using the equation of Sharp and Kirschner (1994) and the average homogenization temperatures from fluid-inclusion studies. The calculated  $\delta^{18}O_{(V-SMOW)}$  values are between -13.5 to -6.4 ‰ and the  $\delta D_{(V-SMOW)}$  values for inclusion waters are between -88 and -62 ‰.

## 5. Discussion

### 5.1. Pressure Temperature Conditions of Mineralization

Constraining the P-T conditions during mineralization can be difficult as the measured homogenization temperatures of fluid inclusions are only minimum temperatures unless there is some way to constrain the pressure. When textural evidence from fluid inclusions for **boiling exists**, this fixes the position on the liquid **vapor** curve for the appropriate salinity. However, this requires the co-existence of fluid inclusions that homogenise to both liquid and **vapor** at the same temperature, but the **vapor** from boiling may not always be trapped. In the earliest generations of quartz at Koru, the  $T_{h_{liq}}$  of fluid inclusions in the growth bands of euhedral quartz (Qz-1) cover a large range of temperatures from c. 260 °C to 360 °C, whereas the  $T_{h_{vap}}$  covers a narrower range from c. 320 °C to 360 °C. Petrographically, the two types of inclusions can be shown to have co-existed. A similar range of  $T_{h_{liq}}$  and  $T_{h_{vap}}$  temperatures were recorded for fluid inclusions in the first generation of sphalerite (Sph-1). These higher homogenization temperature fluid inclusions are clearly primary occurring in, and terminating at the boundaries of the growth zones. The presence in both quartz and sphalerite of L-V and V-rich fluid inclusions in close association and which homogenise over the same temperature range is indicative of boiling. Variable L/V ratios are also commonly observed (see Figs. 5, 6) in fluid inclusion arrays in **both quartz and sphalerite**, which are also indicative of boiling. The morphology of the Qz-1 overgrowths (Fig. 5a) is indicative of near equilibrium quartz deposition by a fluid saturated with respect to silica (Bozkaya and Banks, 2015b) which is consistent with adiabatic cooling.

In Fig. 12, the data of Haas (1971), for the effect of salinity on the temperature-depth **relationships** of a fluid along the boiling curve at hydrostatic pressure, has been used to construct the P-T-depth association of water of different salinities. Using this data and the evidence of fluid boiling in the earliest quartz allows the pressure and depth of mineralization

768  
769  
770 to be constrained by the boiling assemblages of L/V and V-rich fluid inclusions that  
771 homogenize over the same narrow temperature range c. 310 °C to 350 °C. For a lithostatically  
772 pressured system this equates to between c. 600 m to 700 m depth. If the fluid system was  
773 hydrostatically pressured, then depth would be approximately 1700 m. The depth of trapping  
774 should lie between the depth defined by hydrostatic or lithostatic confining pressures. The  
775 lower pressure limit is likely to be above hydrostatic pressure, as this would require  
776 unconstrained fluid connectivity to the surface over a depth of 1700 m, which is unlikely as  
777 additional pressure from some lithostatic load would be present.  
778

779 Trapping of liquid and vapor fluid inclusions from the same generation of fluid (in  
780 growth zones of FIA's and clusters of fluid inclusions) should occur within a narrow  
781 temperature range, largely dictated by the experimental error. For fluid inclusions within the  
782 same FIA or growth band to exhibit a large range in homogenization temperature, as occurs  
783 here, necessitates a process that can produce a range of homogenization temperatures when  
784 trapping fluid inclusions from the same fluid at the same time. The pressure at the temperature  
785 of boiling can be constrained (Fig. 12) at ~140 bars for the upper Th values of c. 340 °C for  
786 the primary L-V and V-L fluid inclusions in both quartz and sphalerite. The pressure for the  
787 lower homogenization temperature values of primary L-V fluid inclusions in Qz-1 and  
788 sphalerite is ~50 bars at c. 265 °C. Petrographically, there is evidence that boiling and  
789 associated cooling was episodic, with clusters of fluid inclusions observed on growth surfaces  
790 of Qz-1 and the growth bands observed in Qz-1 (Fig. 6). Evidence of boiling, is also indicated  
791 by bands of chalcedony associated with euhedral quartz. However, the majority of fluid  
792 inclusions in the quartz overgrowths do not contain FIA's that indicate extensive boiling with  
793 V-L fluid inclusions being largely absent. Rather the variable L/V ratios within FIA's  
794 represent trapping of fluid inclusions as the hydrothermal fluid cooled when the pressure  
795 decreased from lithostatic to near hydrostatic. The lack of extensive boiling during the  
796  
797  
798  
799  
800  
801  
802  
803  
804  
805  
806  
807  
808  
809  
810  
811  
812  
813  
814  
815  
816  
817  
818  
819  
820  
821  
822

827  
828  
829 transition between the two pressure regimes indicates that the decrease in P-T must have been  
830 close to **that of the L-V curve**. In **this instance**, as the pressure **drop did not put** the fluid  
831 significantly into the **vapor field**, **there would not be a large number** of V-L or **V fluid**  
832 **inclusions** produced. The range of homogenization temperatures can be explained as the  
833 earliest fluid to fill the open space of any vein will suffer the greatest pressure drop and  
834 therefore the greatest temperature drop. As the pressure in the open space increases, as more  
835 fluid enters the fracture and minerals **are deposited**, so the drop in temperature **would decrease**.  
836 This would be recorded in fluid inclusions trapped **over a variable** range of pressures and  
837 homogenization temperatures. **Therefore, when the fluid inclusions are trapped during the**  
838 **precipitation of quartz in the vein, (from early to late) is related to the homogenization**  
839 **temperature**. Thus, we suggest that the growth of Qz-1 and sphalerite occurred during periods  
840 when the pressure varied from close to lithostatic to close to hydrostatic with the maximum  
841 amount of quartz growth at the lower pressures when there was open space in the vein  
842 systems.

853  
854  
855  
856  
857  
858  
859 There are **several examples** of planes or trails of fluid inclusions that **appear to be**  
860 completely empty (**effectively full of vapor of** an unknown density with no observable liquid  
861 **phase**) in both sphalerite (Sph-1) and in the cores of the euhedral quartz (Qz-1). The fluid  
862 **inclusions have** a negative crystal shape (Fig. 6) which is distinctly different to the shapes of  
863 other fluid inclusions that are **V-rich, but also** contain a very small observable quantity of  
864 liquid. Thus we suggest these **are the same** as the low density **vapor** (effectively empty) fluid  
865 inclusions recorded at the **Arapuçandere** deposit in the Biga peninsula (Bozkaya and Banks,  
866 2015b) and elsewhere (Sillitoe and Hedenquist, 2003; Moncada, et al., 2012; Shimizu, 2014)  
867 that were generated by flashing. **Flashing is a process** which only occurs if the pressure  
868 decreases rapidly (almost instantaneously) to lower than the hydrostatic pressure. The liquid  
869 in the system does not have time to boil in the conventional manner but is instead

886  
887  
888  
889  
890  
891  
892  
893  
894  
895  
896  
897  
898  
899  
900  
901  
902  
903  
904  
905  
906  
907  
908  
909  
910  
911  
instantaneously converted into vapor and trapped in fluid inclusions where the vapor pressure is very low (effectively empty). Such fluid inclusions are usually preserved as secondary inclusions in pre-existing minerals due to the low Si concentration that would be present in the very low density vapor. Trapping of flashed vapor will only occur if the vein system had a finite volume and was not open to the surface. In this scenario, when the rock fractures due an instantaneous event, almost certainly a tectonic event, the pressure can decrease well below hydrostatic (Sibson, et al., 1988; Weatherley and Henley, 2013; Wilkinson and Johnson, 1996). If however, the vein opening was in response to supra-hydrostatic fluid pressure exceeding the confining strength of the rock then the volume of fluid flooding into the open space would not have allowed the pressure in the veins to drop quickly or low enough to produce flashing as the more rapid influx of fluid would have limited the pressure decrease.

912  
913  
914  
915  
916  
917  
918  
919  
920  
921  
922  
923  
924  
925  
926  
927  
928  
929  
930  
931  
932  
933  
934  
935  
936  
937  
938  
939  
940  
941  
942  
943  
944  
The later generation of fluid inclusions, with lower homogenization temperatures, are present in the second generation of quartz and sphalerite and possibly the first generation of baryte. Fluid inclusions were located in Qz-2 (one sample  $T_{h_{liq}}$  c. 230-250 °C, others  $T_{h_{liq}}$  c. 170-210 °C), Sph-2 ( $T_{h_{liq}}$  c. 130-165°C), Bt-1 ( $T_{h_{liq}}$  c. 120-165 °C, one sample as low as  $T_{h_{liq}}$  c. 70 °C) and finally Bt-2 in which only liquid fluid inclusions are present and is therefore likely to have been trapped at less than c.60°C (as a general rule if fluids were trapped at above c.60°C they should nucleate a vapor bubble on cooling to room temperature). The samples were obtained from present day depths of 40 to 70 m, but the fluid inclusion homogenization temperatures would indicate they were trapped at slightly greater depths. The liquid fluid inclusions in the late barite (Bt-2) would be consistent with fluids derived from the surface. The salinity of these fluid inclusions covers approximately the same range as was recorded in the fluid inclusions trapped in the first generations of quartz and sphalerite (Fig. 9) and therefore these later fluids could simply be cooler fluids from the hydrothermal system expelled upwards and trapped at the same depth as the hotter early fluid inclusions. However,

945  
946  
947 there are a number of fluid inclusions with significantly lower salinities and it is possible **that**  
948 **during** this latest stage of mineralization there was mixing with cooler surface derived fluids  
949  
950  
951 that would fit with final deposition of Bt-2 at less than **c.60°C**.  
952  
953

## 954 955 956 *5.2. Temperature-Salinity Variability*

957  
958 **The high homogenization** temperatures of **primary** fluid inclusions (earliest fluids) in quartz  
959 and sphalerite **have** a large range of salinities from c. 2 to 9 equivalent wt.% NaCl. The data  
960 does not support any visible correlation between homogenization temperature and salinity. In  
961 the lower homogenization temperature fluids (later fluids) there is also no discernible  
962 correlation with salinity. However, **it was proposed** (Çiçek and Oyman, 2016) that there was  
963 such a correlation, with mixing of the higher temperature high salinity fluid (magmatic fluid)  
964 with a lower temperature low salinity fluid (meteoric fluid). This **was also** suggested for other  
965 deposits in the Biga Peninsula (Orgün et al., 2005, Yilmaz, et al, 2010, Çiçek et al., 2012), but  
966 this is supposition and has not been corroborated by other evidence (Banks et al. 2017). In the  
967 previous section, the homogenization temperature variability was shown to be related to  
968 adiabatic cooling of a single hydrothermal fluid as the pressure changed during opening of  
969 faults and fractures. This implies that the variation in salinity would not be due to the presence  
970 of a second fluid and mixing between two different salinity fluids. It would appear fortuitous  
971 that the homogenization temperature decrease caused by fluid mixing would match the  
972 decrease caused by adiabatic expansion of the **fluid as the** pressure **decreased** from lithostatic  
973 to near hydrostatic. Within the individual Qz-1 growth bands (Fig. 6a) **fluid inclusions**, which  
974 are primary, have different L/V ratios and different homogenization temperatures, **but** with a  
975 consistently low salinity. This is likely to **have occurred** by the process we suggested above,  
976 rather than by fluid mixing, which should be homogeneous on the scale of individual growth  
977 bands. We do not see individual growth bands in Sph-1, but we can see variable L/V ratios of  
978  
979  
980  
981  
982  
983  
984  
985  
986  
987  
988  
989  
990  
991  
992  
993  
994  
995  
996  
997  
998  
999

1004  
1005  
1006 fluid inclusions within individual FIA's. Again, on this scale we would expect **fluid inclusions**  
1007 **with** homogeneous L/V ratios from fluid mixing.  
1008  
1009

1010 Deposits in the Biga Peninsula can either have fluid inclusions with a dominantly high  
1011 homogenization temperature and **low salinity**, in the deposits that are gold resources or with  
1012 similar high homogenization temperatures, but a mixed range of salinities, as **we have**  
1013 **presented in this study**, in deposits that are a base-metal resource with lesser amounts of gold  
1014 (Table 1). Low salinity fluid inclusions from the Arapuçandere deposit, which is similar to  
1015 Koru, are interpreted to be derived from magmatic **vapors**, following a study by Banks et al.  
1016 (2019). The high homogenization temperature, low salinity fluids have gold and silver  
1017 concentrations up to 100's of ppm and gold particles **can be observed** in all of the inclusions.  
1018 This would not be possible if the fluids were meteoric. We propose that Koru and other  
1019 deposits in the Biga peninsula, **with the same fluid inclusion characteristics**, may also contain  
1020 gold **colloids** that **were transported by a magmatic fluid**.  
1021  
1022  
1023  
1024  
1025  
1026  
1027  
1028  
1029  
1030  
1031  
1032  
1033  
1034  
1035

### 1036 *5.3. Fluid Compositions*

1037

1038 The low eutectic melting temperatures, between -40 °C and -50 °C, in quartz and  
1039 sphalerite indicates the **fluid inclusions** contain a significant amount of cations, such as Ca in  
1040 addition to NaCl. Most of the **fluid inclusions homogenize to** liquid and account for the  
1041 majority of the salinity data. There was no observable CO<sub>2</sub>, either at room temperature or  
1042 during cooling of the L-V or less common V-**fluid** inclusions. The fluids can therefore be  
1043 considered as variable salinity chloride fluids that are comparable with other deposits in the  
1044 Biga Peninsula. In previous studies of two deposits in the Biga Peninsula (Bozkaya et al.  
1045 2014; Bozkaya and Banks, 2015b) crush-leach **analyses** of fluid inclusions were used as an  
1046 indicator of the source of the fluids, as Cl and Br are predominantly conservative when in  
1047 solution and are not affected by water-rock-interactions, except when evaporites are involved.  
1048  
1049  
1050  
1051  
1052  
1053  
1054  
1055  
1056  
1057  
1058  
1059  
1060  
1061  
1062

1063  
1064  
1065 At both Tesbihdere and Arapuçandere the fluid inclusions have very high Cl/Br and Na/Br  
1066 ratios that are not consistent with either fluids derived from seawater, dissolution of halite or  
1067 meteoric water. Three quartz samples analyzed in this study, using the method of Banks et al.  
1068 (2000), have Cl/Br and Na/Br molar ratios for sample TK-83 (49,000 and 60,000) TK-61  
1069 (33,000 and 22,000) and TK-75 (18,000 and 21,000) that are similar to those recorded form  
1070 the Tesbihdere and Arapuçandere deposits. Values in the thousands for Cl/Br and Na/Br have  
1071 been found in volcanic gases (Pitcairn et al. 2001) and when fluids boil. Chloride  
1072 preferentially goes into the vapor, relative to Br, while Br remains in the liquid (Germann et  
1073 al., 2003). Therefore, the high Cl/Br and Na/Br from Koru are consistent with a low salinity  
1074 vapor derived from a deeper magmatic fluid.

1075  
1076 The cation concentrations of the fluids from the Koru deposit were determined in  
1077 individual fluid inclusions or groups of smaller fluid inclusions in early quartz and sphalerite  
1078 by LA-ICP-MS. Most of the analyzed fluid inclusions were L-V but some V-fluid inclusions  
1079 were also ablated. The fluids are dominated by the alkali and alkaline earth elements with Na  
1080 having the highest concentrations. The element/Na weight ratios are shown in Fig. 10 together  
1081 with the calculated concentrations in Table 3. It should be noted that in Table 3, the K/Na  
1082 ratio was used in the calculations of elemental concentrations in the fluid inclusions as the  
1083  $K^*/Na$  ratio has an elevated concentration of K from the presence and ablation of what we  
1084 interpret to be small crystals of illite.

1085  
1086 The K/Na ratios fall into two groups, one where K/Na is greater than 1, the other  
1087 between c. 0.2 and 0.4. The high ratios ( $K^*/Na$ ) are inconsistent with the homogenization  
1088 temperatures when used to calculate the temperature from mineral-fluid geothermometers  
1089 (Verma and Santoyo, 1997). Such high ratios are not uncommon and are often found  
1090 associated with acid-sulphate alteration zones in high sulfidation hydrothermal systems (Ece  
1091 et al., 2008). However, this is not the case for the Koru deposit which is a low to intermediate

1122  
1123  
1124 sulfidation deposit. We surmise that in fluid inclusions where a solid was not visible but had a  
1125  
1126 high  $K^*/Na$  there would have been a solid present. The most likely mineral is illite, which has  
1127  
1128 been associated with boiling in hydrothermal systems (Moncada et al., 2012). There is no  
1129  
1130 statistical difference (standard t-test) of the individual element/Na ratios of fluid inclusions in  
1131  
1132 quartz, sphalerite or baryte (Fig. 10) which indicates the same fluid was trapped in the  
1133  
1134 different minerals. Although there is a range of salinities, in fluid inclusions trapped in  
1135  
1136 different quartz and sphalerite samples, the element/Na ratios do not have a large range of  
1137  
1138 values **within each sample** and the average value is similar between samples. The presence of  
1139  
1140 the fluid inclusions with a high  $K^*/Na$  value fluid, does not imply a different fluid, only that  
1141  
1142 the presence of a K-bearing mineral was responsible for the additional group of  $K^*/Na$  ratios.  
1143  
1144

1145  
1146 The base metal concentrations of the fluid **inclusions are consistent** with crustal fluids  
1147  
1148 at these temperatures and salinities (Yardley, 2005). The Cu concentration is between c.150  
1149  
1150 and 600 ppm, Zn between c.120 and 300 ppm and Pb between c.110 and 300 ppm. In  
1151  
1152 comparison to other higher temperature magmatic fluids the metal contents in these  
1153  
1154 epithermal fluids are much lower **as would be expected from their lower temperatures**  
1155  
1156 (Audetat et al., 2008; Pudack et al. 2009). The solubility of metal-chloride complexes  
1157  
1158 decreases as temperature is reduced and therefore reduces the amount of metal that can be  
1159  
1160 transported. Other mechanisms of metal precipitation are **the** increase of pH due to wall-rock  
1161  
1162 interaction, or boiling.  
1163  
1164

#### 1165 1166 *5.4. Isotopic Constraints on the Hydrothermal Fluids*

1167

1168  
1169 The distribution of measured and calculated isotopic composition of hydrothermal  
1170  
1171 fluids from the Koru mine, which were in equilibrium with quartz (Fig. 11a), is very close to  
1172  
1173 magmatic values **(5.5-9.5‰ defined by Ohmoto (1986) and Sheppard (1986). The water in**  
1174  
1175 **equilibrium with baryte, which was the last mineral to be precipitated,** was enriched in  
1176  
1177

1181  
1182  
1183 deuterium and had isotopically lighter oxygen **thereby** plotting close to Eastern Mediterranean  
1184 Meteoric Water: (EMMW)  $\delta^{18}\text{O} = -6.12\text{‰}$ ,  $\delta\text{D} = -37.96\text{‰}$  (Gat et al., 1996).  
1185  
1186

1187 The fluid  $\delta^{18}\text{O}$  values calculated from  $\delta^{18}\text{O}_{\text{Bt}}$  are slightly lower than **calculated** for the  
1188  $\delta^{18}\text{O}_{\text{Qz}}$  (Fig. 11b). The difference can be interpreted to indicate that baryte and quartz were  
1189 precipitated at different stages of mineralization. Baryte is often a late-stage mineral in  
1190 hydrothermal systems. Its solubility increases with increasing salinity between 100 and 250  
1191 °C, and for solutions that contain more than 1 mol NaCl (Holland and Malinin, 1979).  
1192 Because **baryte** is precipitated during cooling and especially during the mixing of late-stage  
1193 hydrothermal fluids with meteoric water, it occurs principally on the margins and in the late  
1194 stages of ore deposits (Rye, 2005). In the Koru deposit the petrography indicates baryte was  
1195 precipitated later than quartz at a lower homogenization temperature.  
1196  
1197

1200 The  $^{34}\text{S}_{\text{V-CDT}}$  values of sphalerite, galena and **baryte** from the Koru deposit are  
1201 between -1.9 to -0.1 ‰ (average -1.2 ‰), -5.2 to -3.0 ‰ (average -3.9 ‰) and +14.9 to  
1202 +17.3 ‰ (average +16.5 ‰), respectively (Bozkaya and **Gökçe**, 2009). **The two different**  
1203 ranges of  $\delta^{34}\text{S}$  values for  $\text{H}_2\text{S}$  in equilibrium with baryte and sulfide minerals indicate there  
1204 were different sources **for the sulfur** in sulfides and barytes. The heaviest  $\delta^{34}\text{S}$  values, from  
1205 the second generation of **baryte**, are consistent with  $\text{SO}_4$  derived from Eocene seawater. The  
1206 first generation of baryte has  $\delta^{34}\text{S}$  values which are lower than seawater at the time of  
1207 mineralization **and we suggest** this was caused by micron sized sulfide inclusions, which are  
1208 observed in the baryte and could not be removed prior to analysis. These have much more  
1209 negative  $\delta^{34}\text{S}$  and their presence has **lowered** the **measured**  $\delta^{34}\text{S}$  of baryte **from the correct**  
1210 **values for a derivation from seawater.**  
1211  
1212  
1213  
1214  
1215  
1216  
1217  
1218  
1219  
1220  
1221  
1222  
1223  
1224  
1225  
1226  
1227  
1228  
1229

1230 The distinctly negative  $\delta^{34}\text{S}$  values of galena are lower than for sulfur that had a  
1231 magmatic source. Sulfides in the country rocks with negative  $\delta^{34}\text{S}$  values could have been  
1232 leached by the hydrothermal fluids but there is no evidence of any such sulfides. We suggest  
1233  
1234  
1235

1240  
1241  
1242 that the negative  $\delta^{34}\text{S}$  values of the sulfides are due to boiling of the magmatic fluid at depth.  
1243  
1244 Such a process has been shown to produce very negative  $\delta^{34}\text{S}$  at the surface, such as at White  
1245  
1246 Island, New Zealand (Hedenquist et al. 1993). According to the  $\delta^{34}\text{S}$  and  $\delta^{18}\text{O}$  data of the  
1247  
1248 baryte from Koru (Table 5 and 6; Bozkaya and Gökce, 2009), the positive slope of the sulfur  
1249  
1250 and oxygen–isotope data for **baryte** (Rye 2005) is interpreted to represent mixing of  $\text{SO}_4^{2-}$   
1251  
1252 derived from the disproportionation of magmatic  $\text{SO}_2$  at depth (magmatic-hydrothermal) with  
1253  
1254 sulfate formed during the oxidation of  $\text{H}_2\text{S}$  near the surface (steam-heated).  
1255  
1256

1257 In Fig. 11a, the  $\delta^{18}\text{O}$  and  $\delta\text{D}$  for the fluid inclusions are plotted for deposits in the Biga  
1258  
1259 Peninsula; at **Arapuçandere** (AUD), Balcılar (BA), Tesbihdere- Sahinli (TD-SA) and Ovacik-  
1260  
1261 Narlica (OV-NA). These all **lie** between the meteoric water line and the magmatic box  
1262  
1263 (Bozkaya and Banks, 2015b, Bozkaya and Gökçe, 2007; Yilmaz, 2002; Yilmaz et al., 2010).  
1264  
1265 Meteoric water at the time of mineralization plots close to the value of present day meteoric  
1266  
1267 **water**; therefore all the deposits except Ovacik–Narlica have mixing trajectories that would  
1268  
1269 intersect close to meteoric water at c. 20 Ma. Nevertheless, they do not extend to, or would  
1270  
1271 intersect the magmatic box as the  $\delta\text{D}$  values are too negative. The data for the deposits of  
1272  
1273 Ovacik and Narlica **have**  $\delta^{18}\text{O}_{\text{H}_2\text{O}}$  **values that are not** close to the magmatic box, and the  $\delta\text{D}$   
1274  
1275 values are approximately 50‰ too negative **when** compared to meteoric water at the time of  
1276  
1277 mineralization.  
1278  
1279  
1280

1281 The stable isotope data,  $\delta\text{D}$  and  $\delta^{18}\text{O}$ , of illite from Koru plots close to the magmatic  
1282  
1283 water box indicating that the hydrothermal fluids producing these alteration products were  
1284  
1285 predominantly magmatic (Bozkaya et al., 2016).  $\delta\text{D}$  and  $\delta^{18}\text{O}$  from early quartz indicates a  
1286  
1287 magmatic fluid source and the two generations of baryte have values that go towards the  
1288  
1289 MWL and the values for local waters at the time of mineralization. However, these are not  
1290  
1291 indicative of magmatic-meteoric water mixing but are a function of the cooling of the  
1292  
1293  
1294  
1295  
1296  
1297  
1298

1299  
1300  
1301 magmatic water and equilibration with the alteration products (e.g., Bozkaya et al., 2016). The  
1302  
1303 only evidence of meteoric water comes from the second generation of **baryte**, which lies on  
1304  
1305 the meteoric water line and has  $\delta^{32}\text{S}$  values that are indicative of Eocene seawater.  
1306

1307  
1308 The isotopic signatures **of fluids** can be changed by interaction with igneous rocks,  
1309  
1310 especially at low water/rock ratios (John et al., 2003; Taylor, 1997). Boiling can also affect  
1311  
1312 the original isotopic signature of the hydrothermal fluid as it increases the  $\delta^{18}\text{O}$  and  $\delta\text{D}$  **values**  
1313  
1314 **of fluids** due to fractionation of  $^{16}\text{O}$  and H into the vapor phase (e.g. Alderton and Fallick,  
1315  
1316 2000). There is clear evidence that boiling occurred within the vein systems in the Koru  
1317  
1318 deposit. Even although  $\delta^{18}\text{O}$  values have a narrow **range**, between -8.5 and -1.7 ‰, **the**  $\delta\text{D}$   
1319  
1320 values cover a large range between -90 and -55 ‰. Such low  $\delta\text{D}$  values **can be interpreted to**  
1321  
1322 **have originated from** boiling by either of the two following mechanisms (Imai et al., 1998); 1)  
1323  
1324 a significant degree of vapor **from boiling above** 225 °C, and 2) a vapor phase separated by  
1325  
1326 boiling at lower temperature (below 160 °C for a fractionation larger than 10 ‰). In the  
1327  
1328 former case, a large degree of boiling with Rayleigh fractionation is required to significantly  
1329  
1330 modify the  $\delta\text{D}$  value of liquid as the hydrogen isotopic fractionation factor between the fluid  
1331  
1332 and  $\text{H}_2\text{O}$  **vapor** is small. Greater than 50% boiling is required for a 2‰ of change in  $\delta^{18}\text{O}$   
1333  
1334 value, whereas the observed variation in  $\delta^{18}\text{O}$  values of the hydrothermal **fluid is from** -8.5 to  
1335  
1336 -1.7‰, calculated from  $\delta^{18}\text{O}$  value of quartz **assuming a temperature of** 300°C (Bozkaya et al.  
1337  
1338 2016). Therefore, boiling alone does not account for the measured isotopic variations of  
1339  
1340 hydrothermal fluids. The lack of evidence for fluid mixing between meteoric and magmatic  
1341  
1342 waters (**except in the last stages of baryte precipitation**) in the Koru deposit indicates that a  
1343  
1344 simple cooling model is most likely, as also inferred from the fluid inclusion data. The  
1345  
1346 evidence points to magmatic fluids being the more likely significant source of fluids.  
1347  
1348  
1349  
1350  
1351  
1352  
1353  
1354  
1355  
1356  
1357

## 6. Conclusions

The geologic characteristics of the Koru deposit; geological setting, alteration style of the host rocks, main textures, mineral assemblages along with the fluid inclusion and stable isotope data, indicate that Koru belongs to the class of intermediate sulfidation type epithermal deposit in the sense of Hedenquist et al. (2000), Sillitoe and Hedenquist (2003), Einaudi et al. (2003) and Sillitoe (2010). The epithermal base-metal ( $\pm$  Au) deposit is characterized by moderate to high temperatures and intermediate to low salinities. The highest temperature inclusions are clearly primary occurring in, and terminating at the boundaries of the growth zones. There is evidence of fluid boiling from the presence in both quartz and sphalerite of closely associated L-V (with variable L/V ratios) and V-rich fluid inclusions that homogenise over the same temperature range in a number of fluid inclusion arrays. In the earliest quartz and sphalerite, the Th range of c. 310 to 350 °C equates to c.1700 m for hydrostatic pressure and c. 600 m to 700 m depth for a fluid system at lithostatic pressure. There is also a large decrease in the homogenization temperatures in FIA's without clear evidence of boiling. In these cases, we suggest the pressure reduction in the veins was more gradual, essentially along or close to the L-liquid vapor curve. We also see evidence of vapor fluid inclusions caused by flashing, by a sudden pressure drop to below hydrostatic pressure. Therefore, we suggest there were a number of scenarios that would have caused a decrease of pressure and hence several physical and chemical changes that led to mineral deposition.

As the temperature decrease is due to pressure variation, stable isotope data that was believed to indicate the presence of a significant amount of meteoric water, can in fact be shown to represent a cooling magmatic fluid in equilibrium with the alteration assemblages. There is no clear evidence for extensive fluid mixing with meteoric water during the main stages of mineralization. Instead, we suggest the lower salinity fluids were magmatic vapor that ascended from deeper in the mineralizing system, to shallower depths to produce a low

1417  
1418  
1419 salinity fluid. This **was also** shown in the comparable Arapuçandere deposit, in the Biga  
1420 peninsula, where gold particles are present in the low salinity fluid inclusions (Bozkaya and  
1421 Banks, 2016 Banks et al. 2019). Therefore, in the Biga peninsula base metal deposits may also  
1422 contain gold, **if these** contain the low salinity fluids that are associated with transport of gold.  
1423  
1424 The amount of gold will depend on the volume of magmatic vapor that was produced. In  
1425 either case deposition of the gold or base-metals was controlled by pressure fluctuations and  
1426  
1427 the effect on metal-ligand complexes, pH, temperature and oxidation state.  
1428  
1429  
1430  
1431  
1432  
1433  
1434  
1435

### 1436 **Acknowledgements**

1437  
1438 The authors thank to Engin Çetinbağ and Çanakkale Mining Company for contributions to  
1439 field studies. We also thank to Dr. Peter Kodera and Dr. Honza Catchpole for their  
1440 constructive reviews that improved the manuscript and **to Dr. Ibrahim Uysal for his**  
1441 **constructive comments and editorial handling of the manuscript.**  
1442  
1443  
1444  
1445  
1446  
1447

### 1448 **References**

- 1449  
1450  
1451 Aldanmaz, E., Pearce, J.A., Thirlwall, M.F., Mitchell, J.G., 2000. Petrogenetic evolution of  
1452 late Cenozoic, post-collision volcanism in western Anatolia, Turkey. *J. Volcanol.*  
1453 *Geoth. Res.* 102, 67-95.  
1454  
1455  
1456  
1457 Alderton, D.H.M., Fallick, A.E., 2000. The nature and genesis of gold- silver-tellurium  
1458 mineralization in the Metaliferi Mountains of western Romania. *Econ. Geol.*, 95, 495-  
1459 515.  
1460  
1461  
1462  
1463 Allan, M.M., Yardley, B.W.D., Forbes, L.J., Shmulovich, K.I., Banks, D.A., Shepherd, T.J.,  
1464 2005, Validation of LA-ICP-MS fluid inclusion analysis with synthetic fluid  
1465 inclusions. *Am. Mineral.* 90, 1767–1775.  
1466  
1467  
1468  
1469  
1470  
1471

- 1476  
1477  
1478 Audetat, A., Pettke, T., Heinrich, C.A., Bodnar, R.J., 2008. The composition of magmatic-  
1479 hydrothermal fluids in barren and mineralized intrusions. *Econ. Geol.* 103, 877-908.  
1480  
1481  
1482 Banks, D.A., Giuliani, G., Yardley, B.W.D., Cheilletz, A., 2000. Emerald mineralization in  
1483 Colombia: fluid chemistry and the role of brine mixing. *Min. Deposita* 35, 699-713.  
1484  
1485  
1486 Banks, D.A., Bozkaya, G., Bozkaya, Ö., 2017. Comment on “Origin and evolution of  
1487 hydrothermal fluids in epithermal Pb-Zn-Cu+Au+Ag deposits at Koru and Tesbihdere  
1488 mining districts, Çanakkale, Biga Peninsula, NW Turkey”. *Ore Geol. Rev.* 86, 971-  
1489 976.  
1490  
1491  
1492  
1493  
1494  
1495 Banks, D.A., Bozkaya, G., Bozkaya, Ö., 2019. Direct observation and measurement of Au  
1496 and Ag in epithermal mineralizing fluids. *Ore Geol. Rev.* 111 (in press).  
1497  
1498  
1499  
1500 Barnes, H.L., 1979. *Geochemistry of Hydrothermal Ore Deposits*. Wiley, New York, pp. 236-  
1501 277.  
1502  
1503  
1504 Berger, B.R., Henley, R.W., 2011. Magmatic-vapor expansion and the formation of high-  
1505 sulphidation gold deposits: Structural controls on hydrothermal alteration and ore  
1506 mineralization. *Ore Geol. Rev.* 39, 75-90.  
1507  
1508  
1509  
1510 Bodnar R.J., 1993. Revised equation and table for determining the freezing point depression  
1511 of H<sub>2</sub>O-NaCl solutions. *Geochim. Cosmochim. Acta* 57, 683-684.  
1512  
1513  
1514 Boucher, K., Miskovic, A., Sanchez, M., Baker, T., Hart, C.J.R., Acimaz, C., Arslan, N., Ilgin,  
1515 O., Ozkayhan, M., Yavuz, O., Akyurek, O., 2016. Structural and hydrothermal fluid  
1516 evolution of the Efemçukuru LS- to IS-epithermal Au deposit, western Turkey.  
1517 Mineral Exploration Roundup 2016. Association for Mineral Exploration British  
1518 Columbia, p. 9.  
1519  
1520  
1521  
1522  
1523  
1524  
1525 Bozkaya, G., 2001. *Geology of Koru (Çanakkale) barite bearing lead-zinc deposits*. PhD  
1526 Thesis, Cumhuriyet University [in Turkish with English abstract, unpublished].  
1527  
1528  
1529  
1530  
1531  
1532  
1533  
1534

- 1535  
1536  
1537 Bozkaya, G., Gökçe, A., 2001. Geology, ore petrography and fluid inclusion characteristics of  
1538 the Koru (Çanakkale) Pb-Zn deposits. Cumhuriyet University Bulletin of the Faculty  
1539 of Engineering , Series A, Earth Sci. 18, 55-70.  
1540  
1541  
1542  
1543 Bozkaya, G., Gökçe, A., 2002. Major, trace and rare earth elements geochemistry of the Koru  
1544 (Çanakkale) lead-zinc deposits. Geol. Bull. Turkey 45, 1-17.  
1545  
1546  
1547 Bozkaya, G., Gökçe, A., 2007. Fluid inclusion and isotope geochemistry studies of the  
1548 galena-barite veins in Balcılar (Lapseki-Çanakkale) area. Abstract of 60<sup>th</sup> Geological  
1549 Congress of Turkey, 188-190.  
1550  
1551  
1552 Bozkaya, G., Gökçe, A., 2009. Lead and sulfur isotope studies of the Koru (Çanakkale,  
1553 Turkey) lead-zinc deposit. Turkish J. Earth Sci. 18, 127-137.  
1554  
1555  
1556 Bozkaya, G., Banks, D.A., 2015a. The importance of supersaturated silica deposition for  
1557 base-metal Au–Ag mineralisation in western Turkey. Turkish J. Earth Sci, 24, 99-110.  
1558  
1559  
1560 Bozkaya, G., Banks, D.A., 2015b. Physico-chemical controls on ore deposition in the  
1561 Arapuçandere Pb-Zn-Cu-precious metal deposit, Biga Peninsula, NW Turkey. Ore  
1562 Geol. Rev. 66, 65-81.  
1563  
1564  
1565 Bozkaya, G., Banks, D.A., 2016. Anatomy of a Quartz Crystal: Evidence for Epithermal Gold  
1566 Deposition. 7<sup>th</sup> Geochemistry Symposium 16-18 May 2016, Proceedings Book, p.45.  
1567  
1568  
1569 Bozkaya, G., Banks, D.A., Ozbas, F., Wallington, J., 2014. Fluid processes in the Tesbihdere  
1570 base-metal-Au deposit: implications for epithermal mineralization in the Biga  
1571 Peninsula. Central Eur. J. Geosci. 6, 148-169.  
1572  
1573  
1574 Bozkaya, G., Gökçe, A., Grassineau, N.V., 2008. Fluid inclusion and stable isotope  
1575 characteristics of the Arapuçandere Pb-Zn-Cu deposits, northwest Turkey. Int. Geol.  
1576 Rev. 50, 848-862.  
1577  
1578  
1579 Bozkaya, G., Gökçe, A., Banks, D.A., Bodnar, R.J., 2011. Epithermal mineralization in  
1580 Western Turkey: nature and origin of the fluids. European Current Research on Fluid  
1581  
1582  
1583  
1584  
1585  
1586  
1587  
1588  
1589  
1590  
1591  
1592  
1593

- 1594  
1595  
1596 Inclusions (ECROFI-XXI) Montanuniversität Leoben, Austria, 9-11 August, 2011.  
1597  
1598 Abstracts, p. 52.  
1599  
1600 Bozkaya, G., Sarı, R., Küçükefe, S., Özkümüş, S., Dönmez, C., Bademler, F., Elbi, G.,  
1601  
1602 Durgun, M.B., 2018. Fluid-Inclusion Characteristics of Çatalçam (Soma-Manisa) Au-  
1603  
1604 Pb-Zn-Cu Mineralization. 8<sup>th</sup> Geochemistry Symposium 2-6 May 2018, Proceedings  
1605  
1606 Book, p.148-149.  
1607  
1608  
1609 Bozkaya, Ö., Bozkaya, G., Yalçın, H., Gökçe, A., 2007. Diagenetic, hydrothermal and surface  
1610  
1611 alterations in the Eocene aged pyroclastic rocks in the vicinity of Koru Pb-Zn deposits.  
1612  
1613 13th National Clay Symposium, 12–14 September 2007, Suleyman Demirel  
1614  
1615 University, Isparta, Proceedings, pp. 80–96.  
1616  
1617  
1618 Bozkaya, Ö., Bozkaya, G., Uysal, I.T., Banks, D.A., 2016. Illite occurrences related to  
1619  
1620 volcanic-hosted hydrothermal mineralization in the Biga Peninsula, NW Turkey:  
1621  
1622 implications for the age and origin of the fluids. *Ore Geol. Rev.* 76, 35-51.  
1623  
1624 Çiçek, M., Oyman, T., Özgenç, I., Akbulut, M., 2012. Fluid evolution of the Koru Pb-Zn  
1625  
1626 deposit, Çanakkale (NW-Turkey). International Earth Science Colloquium on the  
1627  
1628 Aegean Region, IESCA-2012 Abstract Book, 1-5 October, p. 158 (Abstract).  
1629  
1630  
1631 Çiçek, M., Oyman, T., 2016. Origin and evolution of hydrothermal fluids in epithermal Pb-  
1632  
1633 Zn-Cu ± Au ± Ag deposits at Koru and Tesbihdere mining districts, Çanakkale, Biga  
1634  
1635 Peninsula, NW Turkey. *Ore Geol. Rev.* 78, 176-195.  
1636  
1637  
1638 Dong, G., Morrison, G., Jaireth, S., 1995. Quartz textures in epithermal veins, Queensland-  
1639  
1640 classification, origin, and implication. *Econ. Geol.* 90, 1841-1856.  
1641  
1642 Ece, Ö.I., Schroeder, P.A., Smilley, M.J., Wampler, J.M., 2008. Acid-sulfate hydrothermal  
1643  
1644 alteration of andesitic tuffs and genesis of halloysite and alunite deposits in the Biga  
1645  
1646 Peninsula, Turkey. *Clay Min.* 43, 281-315.  
1647  
1648  
1649  
1650  
1651  
1652

- 1653  
1654  
1655 Ercan, T., Satir, M., Steinitz, G., Dora, A., Sarifakioglu, E., Adis, C., Walter, H., Yildirim, T.,  
1656  
1657 1995. Characteristics of Tertiary volcanism in the Biga Peninsula and Gökçeada,  
1658  
1659 Bozcaada and Tavsan islands (NW Anatolia), Bull. Miner. Res. Explor. Inst. Turkish  
1660  
1661 117, 55-86 (in Turkish with English abstract).  
1662  
1663  
1664 Einaudi, M.T., Hedenquist, J.W., Inan, E.E., 2003. Sulfidation state of fluids in active and  
1665  
1666 extinct hydrothermal systems: Transitions from porphyry to epithermal environments.  
1667  
1668 Society of Economic Geologists and Geochemical Society 10, 1-50.  
1669  
1670 Gat, J.R., Shemesh, A., Tziperman, E., Hecht, A., Georgopoulos, D., Basturk, O., 1996. The  
1671  
1672 stable isotope composition of waters of the eastern Mediterranean Sea. J. Geophys.  
1673  
1674 Res. 101, 6441-6451.  
1675  
1676  
1677 Germann, K., Luders, V., Banks, D.A., Simon, K., Hoefs, J., 2003. Late Hercynian  
1678  
1679 polymetallic vein-type base metal mineralization in the Iberian Pyrite Belt: fluid  
1680  
1681 inclusion and stable isotope geochemistry (S-O-H-Cl). Min. Deposita 38, 953-967.  
1682  
1683  
1684 Guillong, M., Meier, D.L., Allan, M.M., Heinrich, C.A., Yardley, B.W.D., 2008. Appendix  
1685  
1686 A6: SILLS: A MATLAB-based program for the reduction of laser ablation ICP-MS  
1687  
1688 data of homogeneous materials and inclusions. In: Sylvester, P. (Ed.). Laser Ablation  
1689  
1690 ICP-MS in the Earth Sciences: Current Practices and Outstanding Issues. Vancouver,  
1691  
1692 Mineralogical Association of Canada Short Course 40, 328-333.  
1693  
1694  
1695 Haas, J.L. Jr., 1971. The effect of salinity on the maximum thermal gradient of a  
1696  
1697 hydrothermal system at hydrostatic pressure. Econ.Geol. 66, 940-46.  
1698  
1699  
1700 Haniççi, N., Bozkaya, G., Banks, D.A., Prokofiev, V., Öztaş, Y., 2015. Preliminary  
1701  
1702 microthermometric data from the Kışladağ Au deposit, western Turkey: Porphyry-  
1703  
1704 Epithermal transition? European Current Research Inclusions (ECROFI-XXIII), Leeds  
1705  
1706 – UK, 27-29 June 2015, Extended Abstract Volume, p. 75-76.  
1707  
1708  
1709  
1710  
1711

- 1712  
1713  
1714 Hedenquist, J.W., Simmons S.F., Giggenbach W.F., Eldridge C.S., 1993. White Island, New  
1715  
1716 Zealand, volcanic-hydrothermal system represents the geochemical environment of  
1717  
1718 high-sulphidation Cu and Au deposition. *Geology* 21, 731–734.  
1719  
1720 Hedenquist, J.W., Arribas, A.Jr., Urien-Gonzales, E., 2000. Exploration for epithermal gold  
1721  
1722 deposits. *Society of Economic Geologists, Reviews in Economic Geology*, 13, 245-  
1723  
1724 277.  
1725  
1726 Heinrich, C.A., 2005. The physical and chemical evolution of low-salinity magmatic fluids at  
1727  
1728 the porphyry to epithermal transition: a thermodynamic study. *Mineralium Deposita*,  
1729  
1730 39, 864-889.  
1731  
1732  
1733 Henley, R.W., Berger, B.R., 2011. Magmatic-vapor expansion and the formation of high  
1734  
1735 sulphidation gold deposits: Chemical controls on alteration and mineralization. *Ore*  
1736  
1737 *Geol. Rev.* 39, 63-74.  
1738  
1739 Holland, H.D., Malinin, S.D., 1979, The solubility and occurrence of non-ore minerals, in  
1740  
1741 Barnes, H.L., ed., *Geochemistry of hydrothermal ore deposits*: New York, Wiley  
1742  
1743 Interscience, p. 461-508.  
1744  
1745 Imai, A, Shimazaki, H., Nishizawa, T., 1998. Hydrogen isotope study of fluid inclusions in  
1746  
1747 vein quartz of the Hishikari gold deposits, Japan. *Resource Geol.* 48, 157–170  
1748  
1749  
1750 Hurtig, N.C., Williams-Jones, A.E, 2015. Porphyry-epithermal Au-Ag-Mo ore formation by  
1751  
1752 vapor-like fluids: New insights from geochemical modelling. *Geology* 43, 587-590.  
1753  
1754  
1755 Jankovic, S., 1986. Tethyan Eurasian Metallogenic Belt: relations of mineral associations and  
1756  
1757 their tectonic setting. *Geotectonica et Metallogenia* 10, 99-124.  
1758  
1759  
1760 Jingwen, M., Pirajno, F., Lehmann, B., Maocheng, L., Berzina, A., 2014. Distribution of  
1761  
1762 porphyry deposits in the Eurasian continent and their corresponding tectonic settings. *J.*  
1763  
1764 *Asian Earth Sci.* 79, 576–584.  
1765  
1766

- 1771  
1772  
1773 John, C. M., Mutti, M., Adatte, T., 2003, Mixed carbonate-siliciclastic record on the North  
1774 African margin (Malta)-Coupling of weathering processes and mid Miocene climate.  
1775  
1776  
1777 Geol. Soc. Am. Bull. 115, 217-229.  
1778  
1779  
1780 Landtwing, M.R., Furrer, C., Redmond, P.B., Pettke, T., Guillong, M., Heinrich, C.A. 2010.  
1781  
1782 The Bingham Canyon porphyry Cu-Mo-Au deposit. III. Zoned copper-gold ore  
1783  
1784 deposition by magmatic vapour expansion. Econ. Geol. 105, 91-118.  
1785  
1786 Moncada, D., Bodnar, R.J., 2012. Gangue mineral textures and fluid inclusion characteristics  
1787  
1788 of the Santa Margarita Vein in the Guanajuato Mining District, Mexico. Central Eur. J.  
1789  
1790 Geosci. 4, 300–309.  
1791  
1792 Moncada, D., Mutchler, S., Nieto, A., Reynolds, T.J., Rimstidt, J.D., Bodnar, R.J., 2012.  
1793  
1794 Mineral textures and fluid inclusion petrography of the epithermal Ag–Au deposits at  
1795  
1796 Guanajuato, Mexico: application to exploration. J. Geochem. Explor. 114, 20–35.  
1797  
1798  
1799 Moncada, D., Baker, D., Bodnar, R.J., 2017. Mineralogical, petrographic and fluid inclusion  
1800  
1801 evidence for the link between boiling and epithermal Ag-Au mineralization in the La  
1802  
1803 Luz area, Guanajuato Mining District, México. Ore Geol. Rev. 89, 143-170.  
1804  
1805 Ohmoto, H., 1986. Stable isotope geochemistry of ore deposits. In: Valley, J.W., Taylor Jr.,  
1806  
1807 H.P., O’Neil, J.R. (Eds.), Stable Isotopes in High Temperature Geological Processes,  
1808  
1809 Rev. Mineral. 16, 491-559.  
1810  
1811 Okay, A.I., Siyako, M., Burkan, K.A., 1990. Geology and tectonic evolution of the Biga  
1812  
1813 Peninsula. Turk. Assoc. Pet. Geol. Bull. 2, 83-121 (in Turkish with English abstract).  
1814  
1815 Okay, A.I., Siyako, M., Burkan, K.A., 1991, Geology and tectonic evolution of the Biga  
1816  
1817 Peninsula. Special Issue on Tectonics (ed. J.F. Dewey), Bulletin of the Technical  
1818  
1819 University of Istanbul 44, 191-255.  
1820  
1821  
1822  
1823  
1824  
1825  
1826  
1827  
1828  
1829

- 1830  
1831  
1832  
1833  
1834  
1835  
1836  
1837  
1838  
1839  
1840  
1841  
1842  
1843  
1844  
1845  
1846  
1847  
1848  
1849  
1850  
1851  
1852  
1853  
1854  
1855  
1856  
1857  
1858  
1859  
1860  
1861  
1862  
1863  
1864  
1865  
1866  
1867  
1868  
1869  
1870  
1871  
1872  
1873  
1874  
1875  
1876  
1877  
1878  
1879  
1880  
1881  
1882  
1883  
1884  
1885  
1886  
1887  
1888
- Orgün, Y., Gultekin, A.H., Onal, A., 2005. Geology, mineralogy and fluid inclusion data from the Arapucan Pb-Zn-Cu-Ag deposit, Çanakkale, Turkey. *J. Asian Earth Sci.* 25, 629-642.
- Oyman, T., Minareci, F., Piskin, Ö., 2003. Efemcukuru B-rich epithermal gold deposit (Izmir, Turkey). *Ore Geol. Rev.* 23, 35-53.
- Pitcairn, I., Banks, D.A., Benning, L.G., Shinohara, H., Goff, F., 2001.  $\delta^{37}\text{Cl}$  and Cl/Br systematics of volcanic gases. *Water-Rock Interaction* 10, 903-906.
- Pokrovski, G.S., Borisova, A.Y., Harrichoury, J.C., 2008, The effect of sulfur on vapor-liquid partitioning of metals in hydrothermal systems. *Earth Planet. Sci. Letters* 28, 345-362.
- Pudack, C., Halter, W.E., Heinrich, C.A., Pettke, T., 2009, Evolution of magmatic vapor to gold-rich epithermal liquid: The porphyry to epithermal transition at Nevados de Famatina, northwest Argentina. *Econ. Geol.* 104, 449-477.
- Rottier, B., Kouzmanov, K., Casanova, V., Walle, M., Fontbote, L., 2018. Cyclic dilution of magmatic metal-rich hypersaline fluids by magmatic low salinity fluid: A major process generating the giant epithermal polymetallic deposit of Cerro de Pasco, Peru. *Econ. Geol.* 113, 825-856.
- Rye, R.O., 2005. A review of the stable-isotope geochemistry of sulfate minerals in selected igneous environments and related hydrothermal systems. *Chem. Geol.* 215, 5-36.
- Sharp, Z.D., Kirschner, D.L., 1994. Quartz-calcite oxygen isotope thermometry: a calibration based on natural isotopic variations. *Geochim. Cosmochim. Acta* 58, 4491-4501.
- Sheppard, S.M.S., 1986. Characterization and isotopic variations of natural waters, in Valley, J. W., Taylor, H. P., Jr., O'Neil, J. R. (Eds.), *Stable isotopes in high-temperature geological processes: Mineralogical Society of America, Reviews in Mineralogy* 16, 165-183.

- 1889  
1890  
1891 Shimizu, T., 2014. Reinterpretation of quartz textures in terms of hydrothermal fluid  
1892 evolution at the Koryu Au-Ag deposit, Japan. *Econ. Geol.* 109, 2051-2065.  
1893  
1894  
1895 Sibson, R.H., Robert, F., Poulson, K.H., 1988. High-angle reverse faults, fluid pressure cycling,  
1896 and mesothermal gold-quartz deposits. *Geology* 16, 551-555.  
1897  
1898  
1899 Sillitoe, R.H., 2010. Porphyry copper systems. *Econ. Geol.* 105, 3-41.  
1900  
1901 Sillitoe, R.H., Hedenquist, J.W., 2003. Linkages between volcanotectonic settings, ore-fluid  
1902 compositions, and epithermal precious-metal deposits. In: Simmons, S.F., Graham, I.  
1903 (Eds.), *Volcanic, geothermal, and ore-forming fluids: rulers and witnesses of*  
1904 *processes within the earth.* Society of Economic Geologists Special Publication. 10,  
1905 315-343.  
1906  
1907  
1908  
1909  
1910  
1911  
1912 Siyako, M., Burkan, K.A., Okay, A.I., 1989. Tertiary geology and hydrocarbon potential of  
1913 the Biga and Gelibolu Peninsulas. *Turkish Assoc. Pet. Geol. Bull.* 1/3, 183-199.  
1914  
1915  
1916  
1917 Spycher, N.F., Reed, M.H., 1989. Evolution of a Broadlands-type epithermal ore fluid along  
1918 alternative P–T paths: implications for the transport and deposition of base, precious,  
1919 and volatile metals. *Econ. Geol.* 84, 328-359.  
1920  
1921  
1922  
1923 Taylor, H.P., 1997. Oxygen and Hydrogen Isotope Relations in Hydrothermal Mineral  
1924 Deposits, In: *Geochemistry of Hydrothermal Ore Deposits*, New York, Wiley. 229-  
1925 302.  
1926  
1927  
1928  
1929 Thiersch, P.C., Williams-Jones, A.E., Clark, J.R., 1997. Epithermal mineralization and ore  
1930 controls of the Shasta Au–Ag deposit, Toadoggonne District, British Columbia, Canada.  
1931 *Miner. Deposita* 32, 44-57.  
1932  
1933  
1934  
1935 Tufan, M., Bozkaya, G., Bozkaya, Ö., Banks, D.A., 2018. Fluid inclusion studies in Tepeoba  
1936 (Balıkesir-Edremit) Cu-Mo deposit. 8<sup>th</sup> *Geochemistry Symposium*, 2-6 May 2018,  
1937 *Proceedings Book*, p. 168-169.  
1938  
1939  
1940  
1941  
1942  
1943  
1944  
1945  
1946  
1947

- 1948  
1949  
1950 Ulrich, M.R., Bodnar, R.J., 1988. Systematics of stretching of fluid inclusions II: barite at 1  
1951 atm confining pressure. *Econ. Geol.* 83, 1037-1046.  
1952  
1953  
1954 Unal, E.I., Guleç, N., Kuşcu, I., Fallick, A.E., 2013. Genetic investigation and comparison of  
1955 Kartaldağ and Madendağ epithermal gold deposits in Çanakkale, NW Turkey. *Ore*  
1956 *Geol. Rev.* 53, 204-222.  
1957  
1958  
1959 Verma, S.P., Santoyo E., 1997. New improved equations for Na/K, Na/Li and SiO<sub>2</sub>  
1960 geothermometers by outlier detection and rejection. *J Volcanol. Geotherm. Res.* 79, 9-  
1961 24.  
1962  
1963 Vural, A., 2006. Investigation of gold enrichments in Bayramiç (Çanakkale) and its  
1964 surroundings, Ph.D. Thesis, Ankara University [in Turkish with English abstract].  
1965  
1966  
1967 Weatherley, D.K., Henley, R.W., 2013. Flash vaporization during earthquakes evidenced by  
1968 gold deposits. *Nature Geoscience* 6, 294-298.  
1969  
1970  
1971 Whitney, D.L., Evans, B.W., 2010. Abbreviations for names of rock-forming minerals. *Am.*  
1972 *Mineral.* 95, 185-187.  
1973  
1974  
1975 Wilkinson, J.J., Johnson, J.D., 1996. Pressure fluctuations, phase separation, and gold  
1976 precipitation during seismic fracture propagation. *Geology.* 24, 395-398.  
1977  
1978  
1979 Yardley, B.W.D., 2005. 100th anniversary special paper: metal concentrations in crustal fluids  
1980 and their relationship to ore formation. *Econ. Geol.* 100, 613-632.  
1981  
1982  
1983 Yigit, O., 2006. Gold in Turkey-a missing link in Tethyan metallogeny. *Ore Geol. Rev.* 28,  
1984 147-179  
1985  
1986  
1987 Yigit, O., 2012, A prospective sector in the Tethyan Metallogenic Belt: Geology and  
1988 geochronology of mineral deposits in the Biga Peninsula, NW Turkey. *Ore Geol. Rev.*  
1989 46, 118-148.  
1990  
1991  
1992  
1993  
1994  
1995  
1996  
1997  
1998  
1999 Yilmaz, H., 2002. Ovacik gold deposit: an example of quartz-adularia type gold  
2000 mineralization in Turkey. *Econ. Geol.* 97, 1829-1839.  
2001  
2002  
2003  
2004  
2005  
2006

2007  
2008  
2009  
2010  
2011  
2012  
2013  
2014  
2015  
2016  
2017  
2018  
2019  
2020  
2021  
2022  
2023  
2024  
2025  
2026  
2027  
2028  
2029  
2030  
2031  
2032  
2033  
2034  
2035  
2036  
2037  
2038  
2039  
2040  
2041  
2042  
2043  
2044  
2045  
2046  
2047  
2048  
2049  
2050  
2051  
2052  
2053  
2054  
2055  
2056  
2057  
2058  
2059  
2060  
2061  
2062  
2063  
2064  
2065

Yilmaz, H., 2003. Exploration at the Kusçayiri Au (Cu) prospect and its implications for porphyry-related mineralization in western Turkey. *J. Geochem. Explor.* 77, 133-150.

Yilmaz, H., Oyman, T., Arehart, G.B., Colakoglu, A.R., Billor, Z., 2007. Low-sulfidation type Au–Ag mineralization at Bergama, Izmir, Turkey. *Ore Geol. Rev.* 32, 81-124.

Yilmaz, H., Oyman, T., Sonmez, F.N., Arehart, G.B., Billor, Z., 2010. Intermediate sulfidation epithermal gold-base metal deposits in Tertiary subaerial volcanic rocks, Sahinli/ Tespihdere (Lapseki/western Turkey). *Ore Geol. Rev.* 37, 236-258.

Yilmaz, H., Sonmez, F.N., Akay, E., Sener, A.K., Tufan, S.T., 2013. Low-sulfidation epithermal Au-Ag mineralization in the Sindirgi District, Balikesir Province, Turkey. *Turkish J. Earth Sci.* 22, 485-522.

2066  
2067  
2068 **TABLE CAPTIONS**  
2069  
2070

2071 **Table 1.** General characteristics of selected epithermal ore deposits in western and  
2072 northwestern Turkey.  
2073  
2074

2075  
2076 **Table 2.** Summary of the microthermometry data for inclusions from the Koru deposit.  
2077

2078  
2079 **Table 3.** LA-ICP-MS analyses of individual fluid inclusions. Average element ratios (wt/wt  
2080 relative to Na) and concentrations in ppm.  
2081  
2082

2083  
2084 **Table 4.** Oxygen and hydrogen isotope data and calculated  $\delta^{18}\text{O}$  values for inclusion water in  
2085 equilibrium with baryte and quartz from Koru samples. Data for quartz is taken from Bozkaya  
2086 et al. (2016).  
2087  
2088  
2089

2090  
2091  
2092  
2093  
2094 **FIGURE CAPTIONS**  
2095

2096  
2097 **Fig. 1.** (a) Location of the Biga Peninsula in relation to the boundaries of the major tectonic  
2098 plates and Tethyan Eurasian Orogenic Metallogenic Belt (Jingwen et al., 2014), NAF: North  
2099 Anatolian Fault, EAF: East Anatolian Fault, (b) Simplified regional geological map of the  
2100 Biga Peninsula (modified from Siyako et al. 1989; Okay et al. 1990) and radiometric ages of  
2101 volcanic and plutonic rocks and alteration related mineralizations (Ercan et al., 1995;  
2102 Aldanmaz et al., 2000, Yigit, 2012).  
2103  
2104  
2105  
2106  
2107

2108  
2109  
2110 **Fig. 2.** Geology map of the close surrounding area of the sectors in Koru deposits (Bozkaya,  
2111 2001) and cross section of the Tahtalıkuyu and Eskikışla sectors and sample locations.  
2112  
2113

2114  
2115 **Fig. 3.** Photomicrographs of transmitted (a-b) and reflected-plain polarized (c-f) light images  
2116 of the representative ore samples from Koru Deposit. (a) Volcanic rock fragments (VRF) and  
2117 plagioclase (Pg) crystals within the silicified and argillised volcanic matrix of lithic ash tuff  
2118  
2119  
2120

2125  
2126  
2127 from Adadagi Pyroclastics (KR-123, polarised light), (b-c) Plagioclase and/or sanidine  
2128  
2129 pseudomorphs replaced by coarse-grained of quartz crystals related to intense silicification  
2130  
2131 within the radially devitrified (silicified and argillised) volcanic groundmass (TK-66, gallery  
2132  
2133 of Tahtalıkuyu sector, d-crossed polars, e-polarised light), (d) Brecciated and disaggregated  
2134  
2135 sphalerites (Sph) within the galena (Gln) crystals, and sutured boundary relationships between  
2136  
2137 quartz-rich gangue and galena minerals (TK-82, gallery of Tahtalıkuyu sector, 96 level), (e)  
2138  
2139 Anhedra galena crystals were replaced by sphalerite and chalcopyrite (Cpy) (TK-88, gallery  
2140  
2141 of Tahtalıkuyu sector, 150 level), (f) Chalcopyrites containing sphalerite and galena  
2142  
2143 inclusions (TK-245, gallery of Tahtalıkuyu sector, 83 level), (g) Rod-like tennantite (Tnt)  
2144  
2145 separations within the galena (EK-5, **Eskikişla** sector), (h-i) Coarse-grained comb texture  
2146  
2147 euhedral baryte crystals (Bt) within the anhedra quartz and calcite (Cal) crystals (TK-43,  
2148  
2149 gallery of Tahtalıkuyu sector, 150 level, a-crossed polars, b-polarised light).

2150  
2151  
2152 **Fig. 4.** Paragenetic succession of ore and gangue minerals of Koru deposit.

2153  
2154  
2155  
2156  
2157 **Fig. 5.** Different generations of ore minerals and gangue minerals in comb texture of veins in  
2158  
2159 Koru deposit. Primary fluid inclusion in sphalerite (Sph 2), Liquid rich inclusions in baryte  
2160  
2161 (Ba2), in quartz (Q2) L-V inclusions through to growth zone in baryte (Ba1) L-V inclusions  
2162  
2163 with ore stage.

2164  
2165  
2166 **Fig. 6.** Fluid inclusion textures and types. (a) Euhedral overgrowths of quartz delineated by  
2167  
2168 bands of primary inclusions oriented perpendicular to the crystal faces, (b) Variable L/V  
2169  
2170 ratios and often contain V-rich inclusions, (c) The first generation inclusions (L-V) in  
2171  
2172 sphalerites, (d) Coarse-grained baryte observed cutting the second generation of quartz, (e-f)  
2173  
2174 Co-existing V-rich and L-V inclusions and inclusions containing semi-prismatic solids which  
2175  
2176 would appear to have been trapped during boiling, (g) Pseudo secondary and secondary  
2177  
2178 inclusions including L-only, (h) L-V inclusions with same arrays as L-only inclusions, (i-j) L-

2184  
2185  
2186 only inclusions in baryte replaced the euhedral quartz.  
2187  
2188

2189 **Fig. 7.** Homogenization temperatures for the different generations of quartz, sphalerite and  
2190 baryte. Two distinct temperature ranges are evident.  
2191  
2192

2193 **Fig. 8.** Homogenization temperatures of different generation minerals; early and late quartz,  
2194 sphalerite and baryte from Koru Deposit.  
2195  
2196

2197 **Fig. 9.** Homogenization and salinity (equiv. NaCl wt.) of primary and secondary inclusions  
2198 from different generation minerals from Koru deposit.  
2199  
2200

2201 **Fig. 10.** LA-ICP-MS data as wt/wt ratios relative to Na (value 1) from inclusions in the first  
2202 generation of quartz and sphalerite. K/Na has a bimodal distribution but overall the element  
2203 ratios are the same in both minerals.  
2204  
2205

2206 **Fig. 11.** (a) Distribution of hydrogen- and oxygen-isotopic values from the fluid trapped in  
2207 quartz and baryte crystals on the  $\delta D$  vs  $\delta^{18}O$  diagram (diagram was reproduced from  
2208 Sheppard, 1986). Illite oxygen isotope data (Bozkaya et al., 2016) is also added for  
2209 comparison. Fluid compositional areas (BA: Balcılar, AUD: Arapuçandere, OV-NA: Ovacık-  
2210 Narlıca, TD-SA: Tesbihdere-Şahinli) are given from Bozkaya and Gökçe, 2007 (BA),  
2211 Bozkaya and Banks, 2015 (AUD), **Yilmaz** et al., 2010 (TD-SA) and **Yilmaz**, 2002 (OV-NA).  
2212 (b) Oxygen isotopic change of waters in equilibrium with quartz and barytes at decreasing  
2213 temperatures. Illite oxygen isotopic changes (Bozkaya et al., 2016) were also added for  
2214 comparison.  
2215  
2216  
2217  
2218  
2219  
2220  
2221  
2222  
2223  
2224  
2225  
2226  
2227  
2228  
2229  
2230

2231 **Fig. 12.** Pressure-Temperature-Depth plot for Koru deposit (drawn from data in Haas, 1971).  
2232  
2233  
2234  
2235  
2236  
2237  
2238  
2239  
2240  
2241  
2242

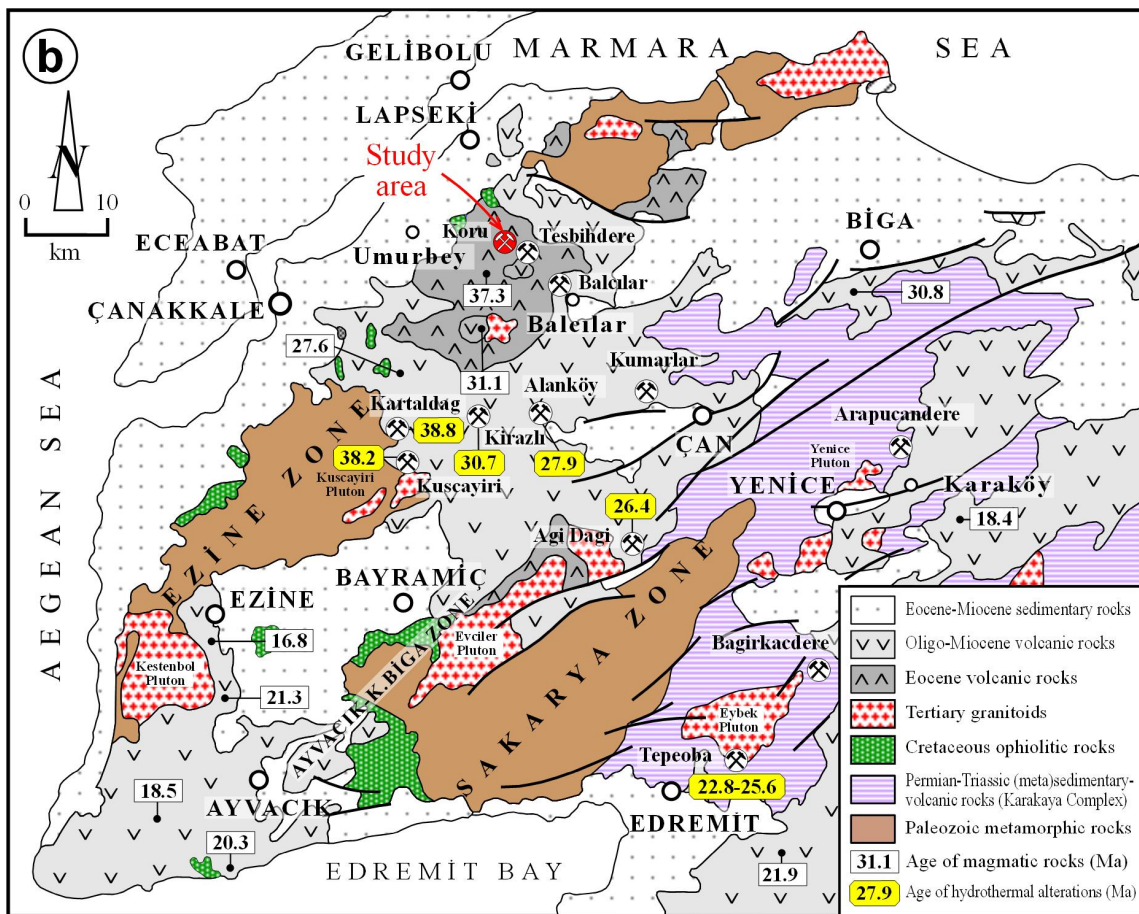
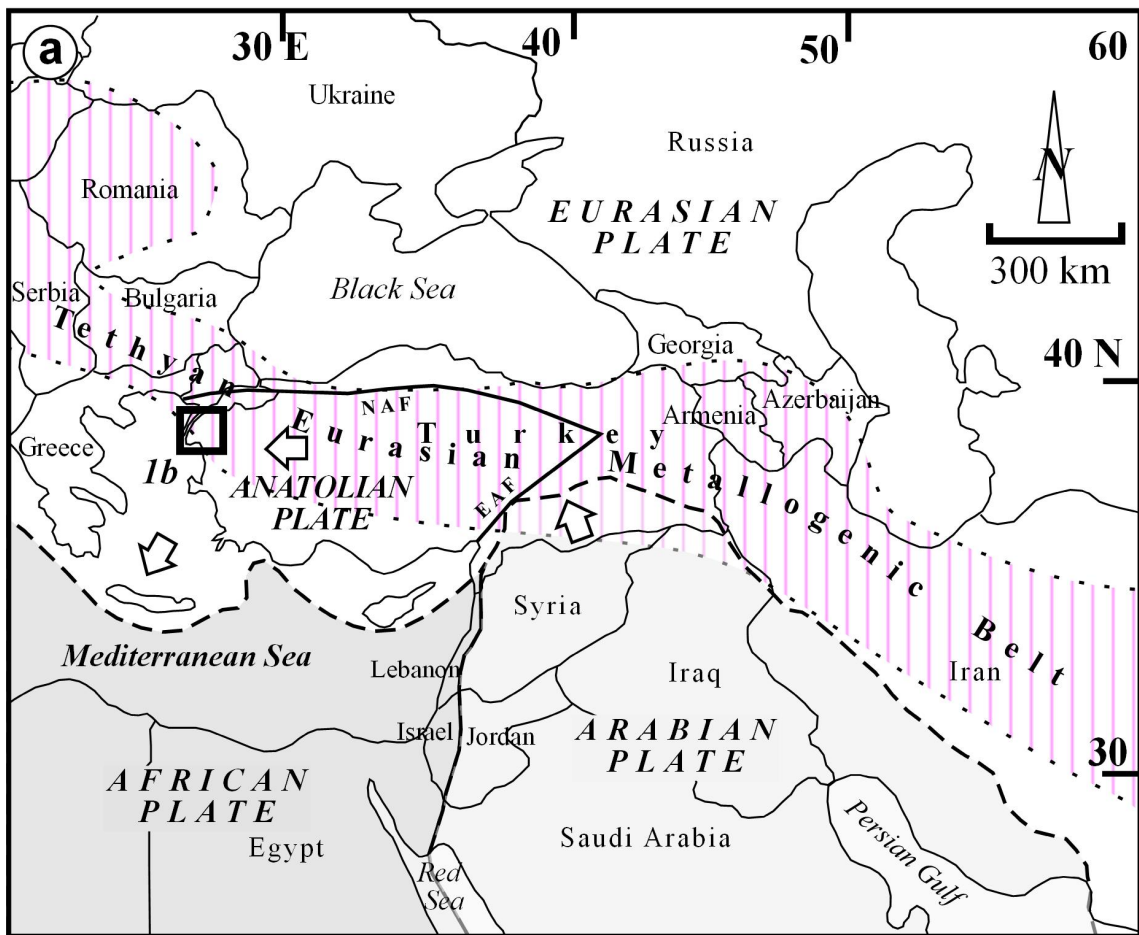


Figure 1-R1

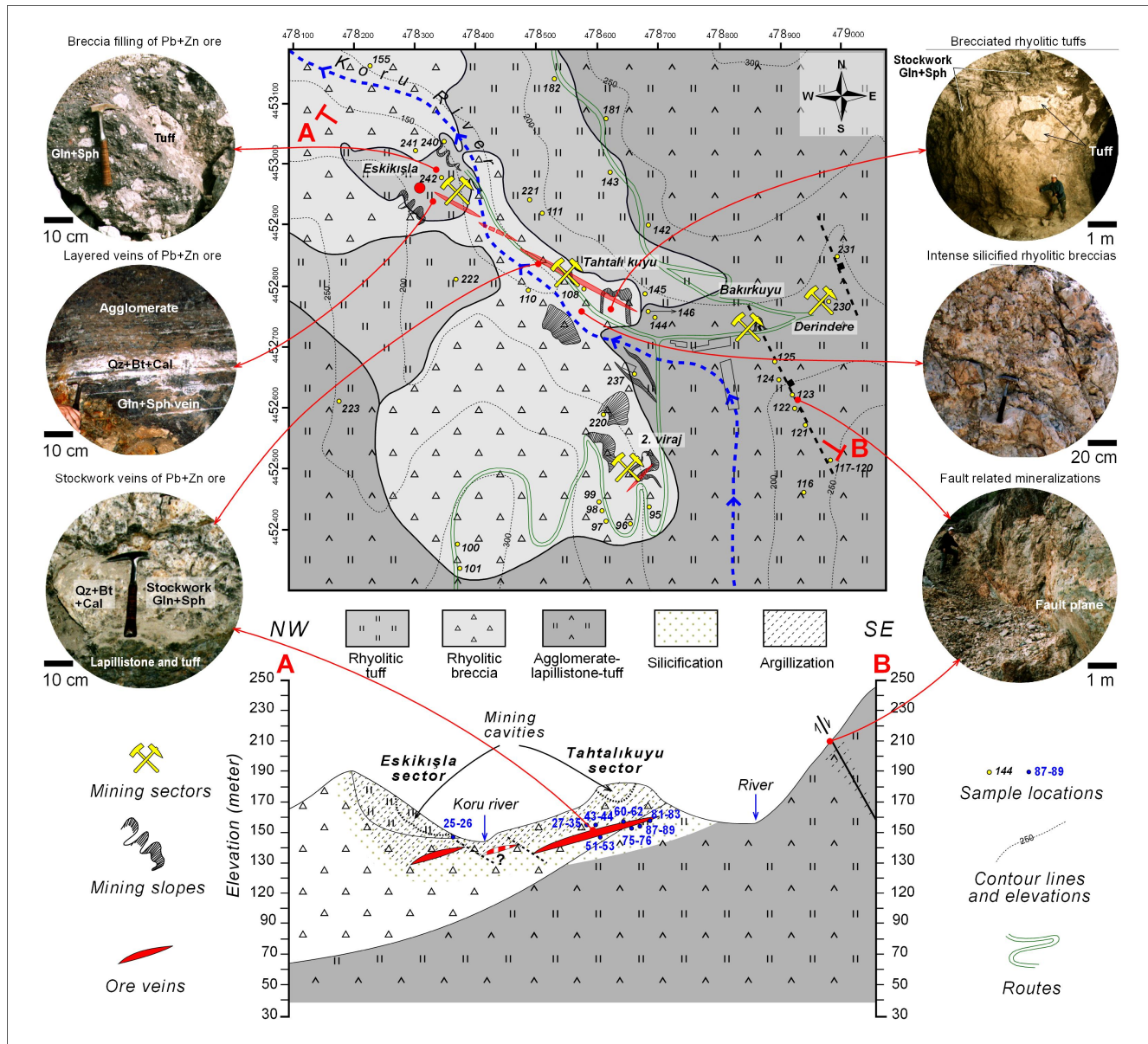


Figure 2-R1

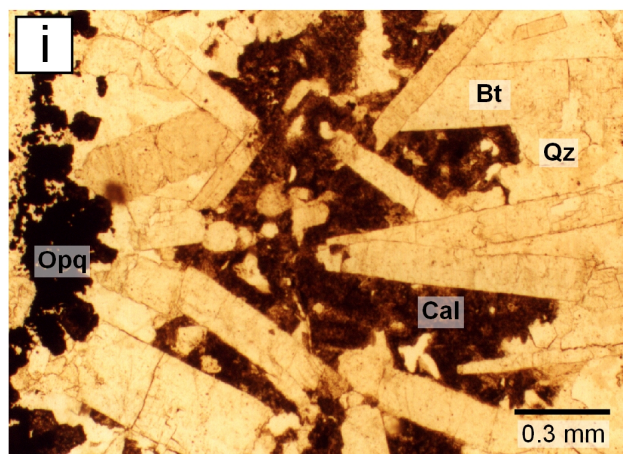
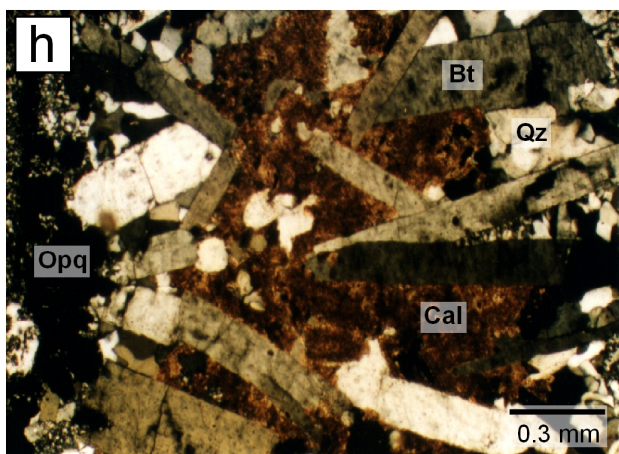
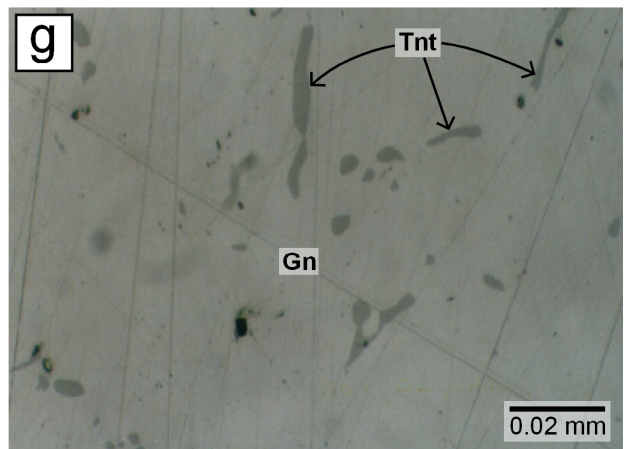
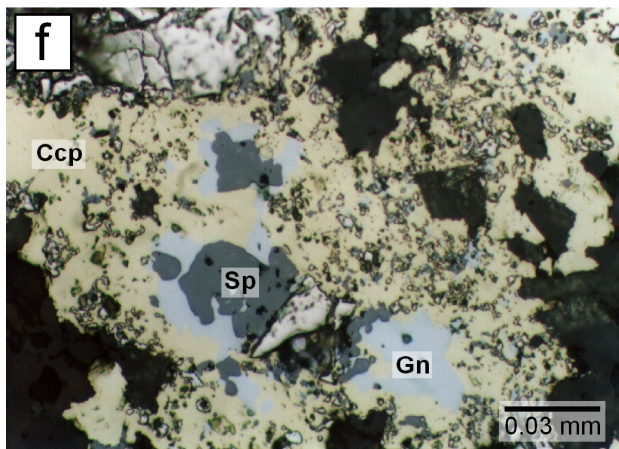
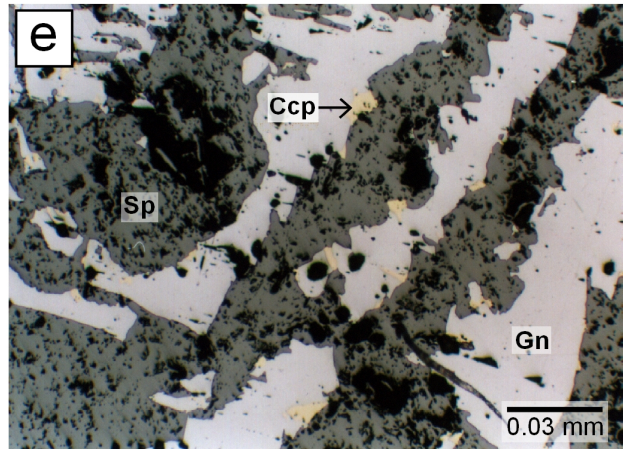
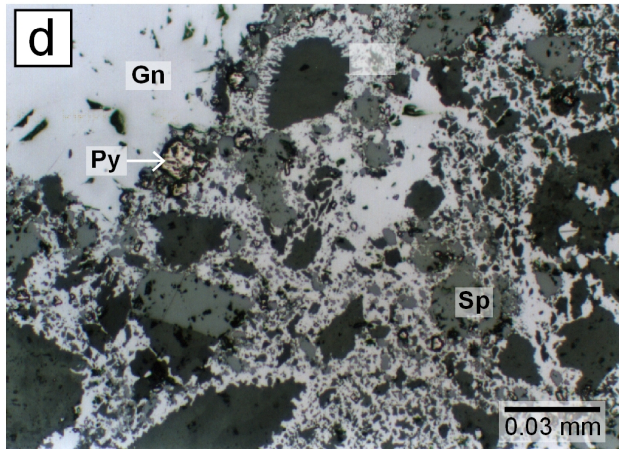
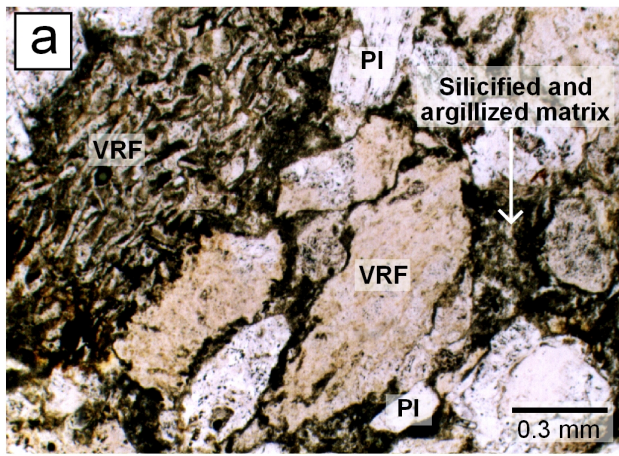


Fig. 3-R2

Mineral	Hydrothermal			Supergene
	Stage-1	Stage-2	Stage-3	Stage-4
Pyrite	—①—		—②—	
Galena		—①—	—②—	
Sphalerite		—①—	—②—	
Chalcopyrite		—①—	—②—	
Fahlore			————	
Bornite			————	
Marcasite			————	
Quartz		—①—	—②—	
Baryte			—①—	—②—
Calcite				————
Chalcocite				————
Covellite				————
Tenorite				————

Fig. 4-R1

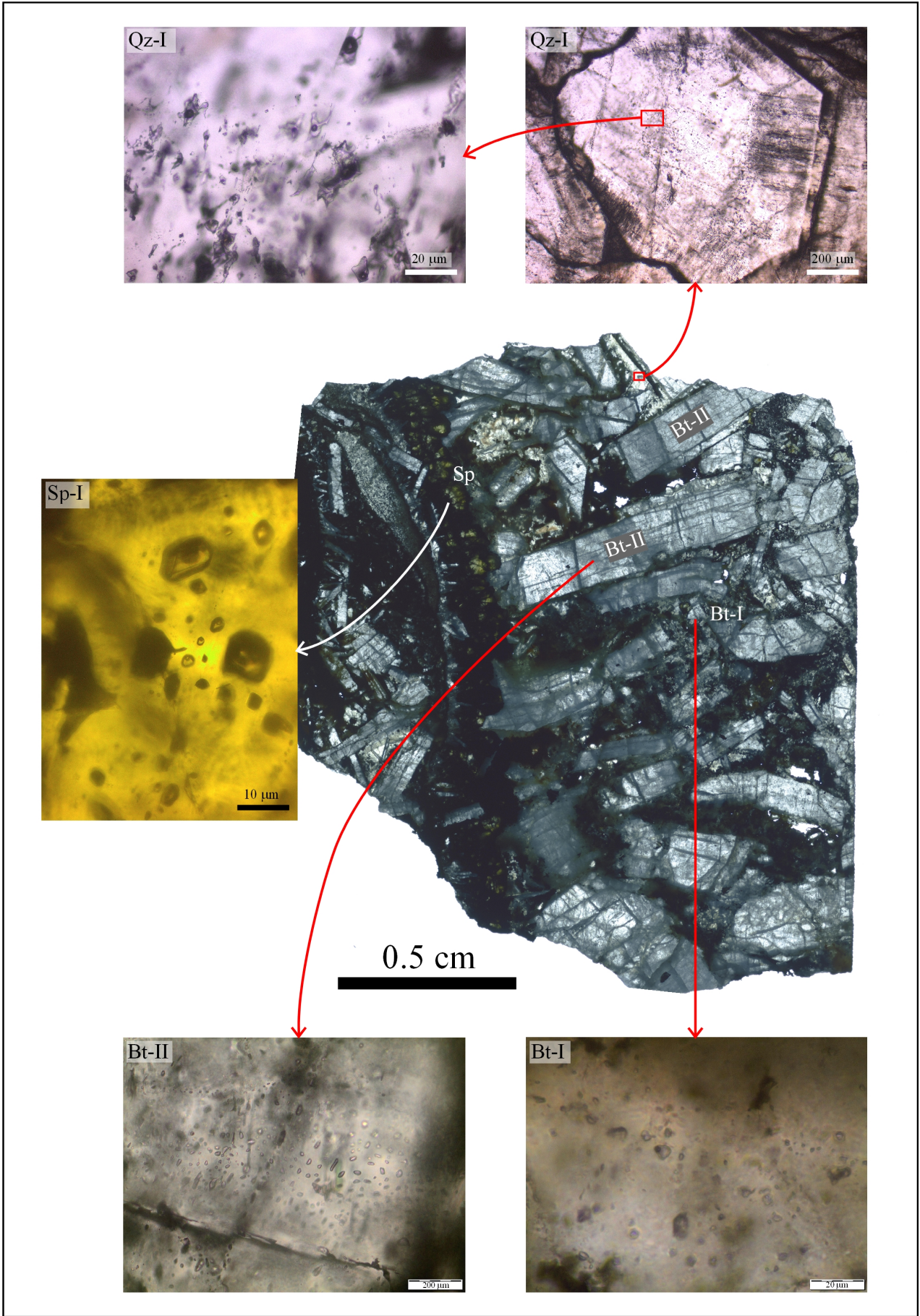


Figure 5-R2

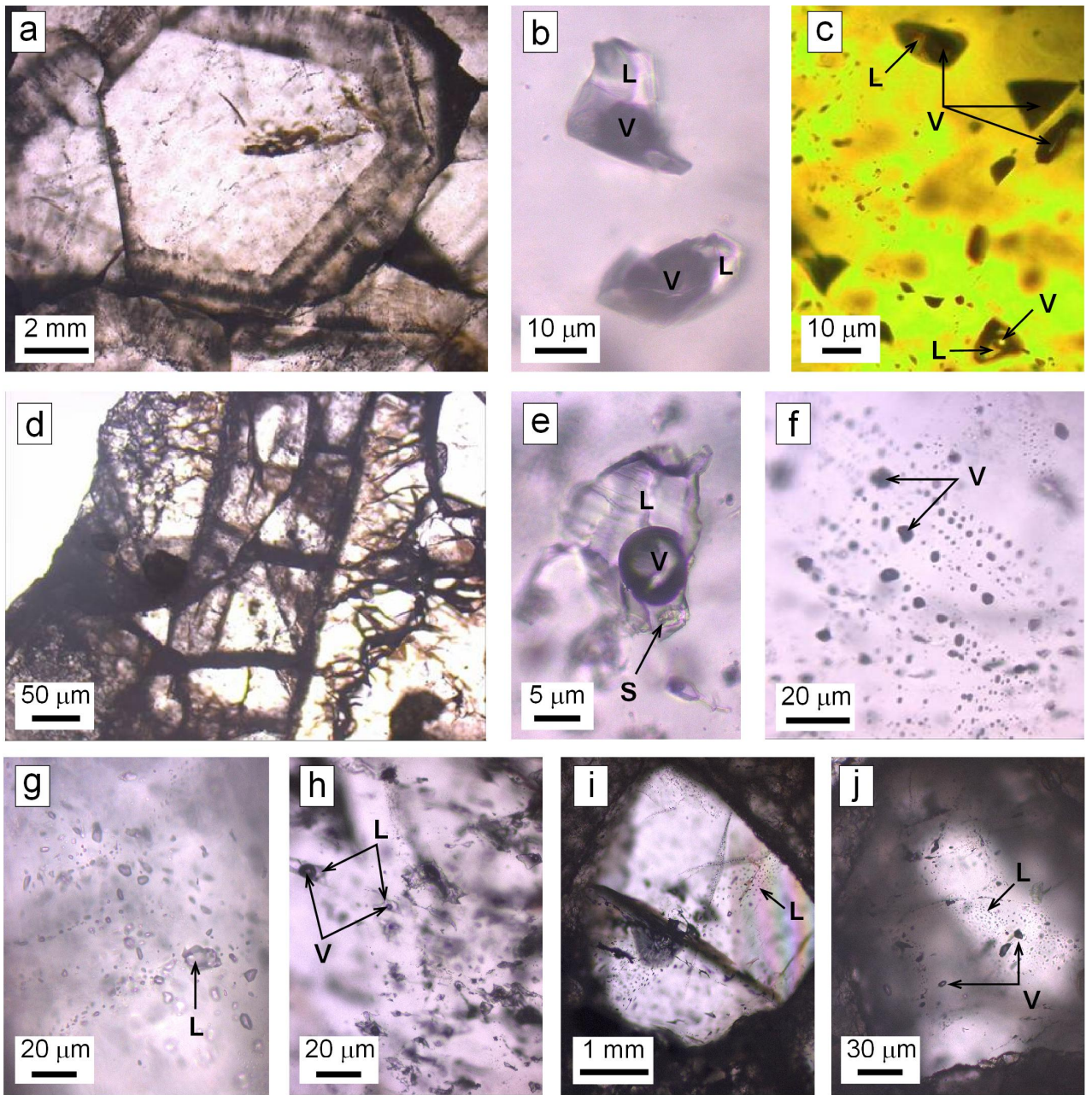


Figure 6-R1

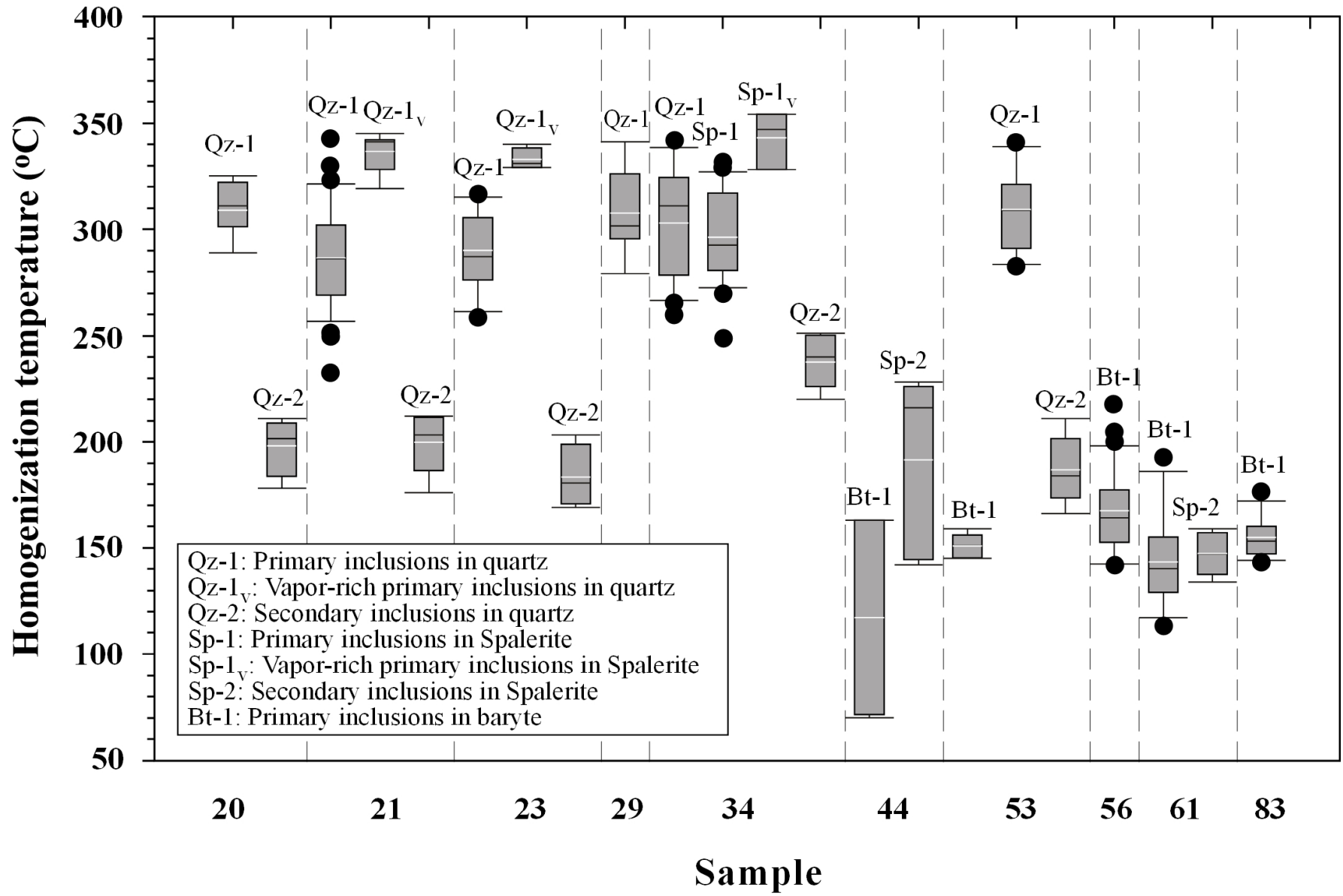


Figure 7-R2

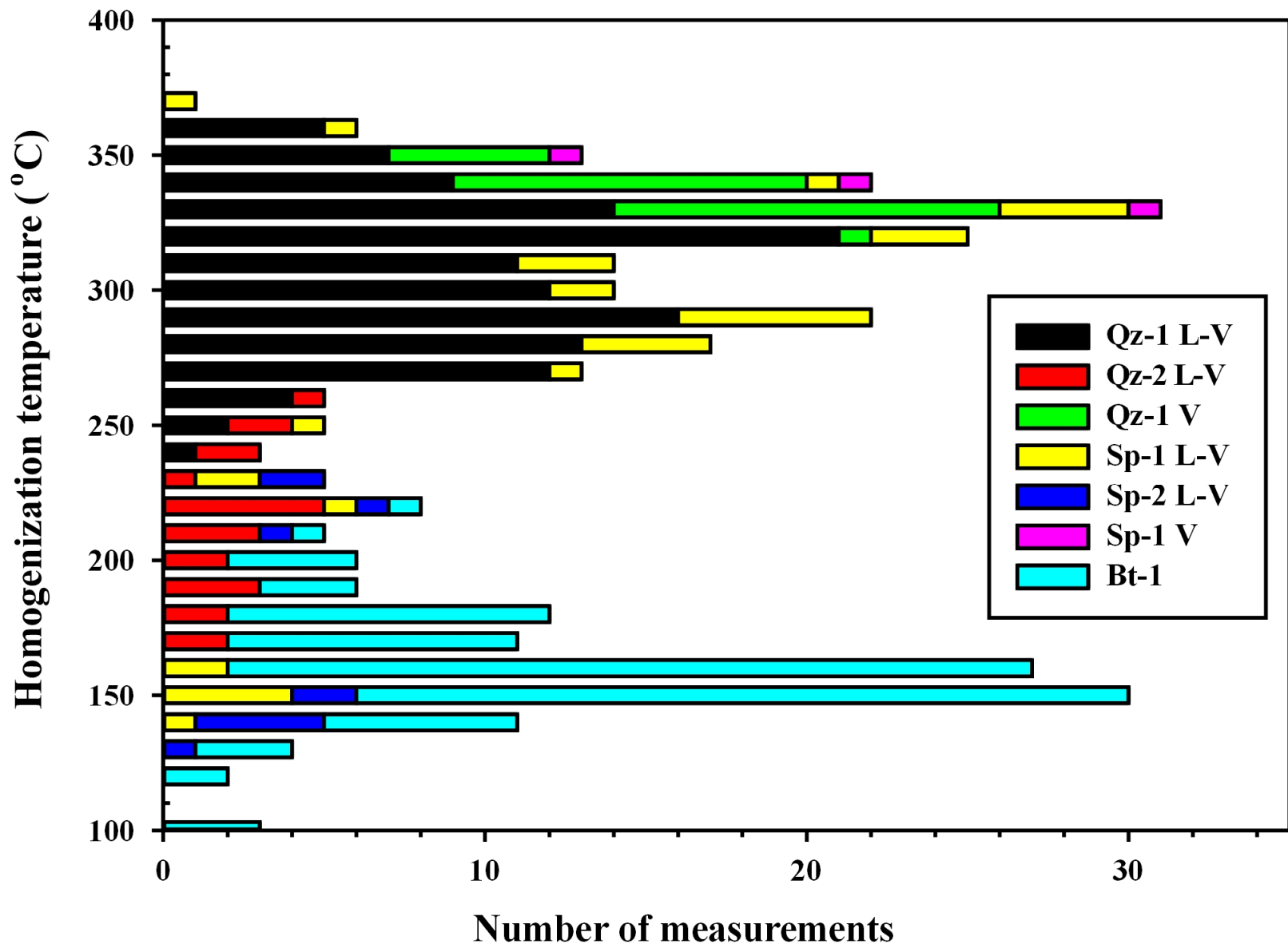


Fig. 8-R2

1  
2  
3  
4  
5  
6  
7  
8  
9  
10  
11  
12  
13  
14  
15  
16  
17  
18  
19  
20  
21  
22  
23  
24  
25  
26  
27  
28  
29  
30  
31  
32  
33  
34  
35  
36

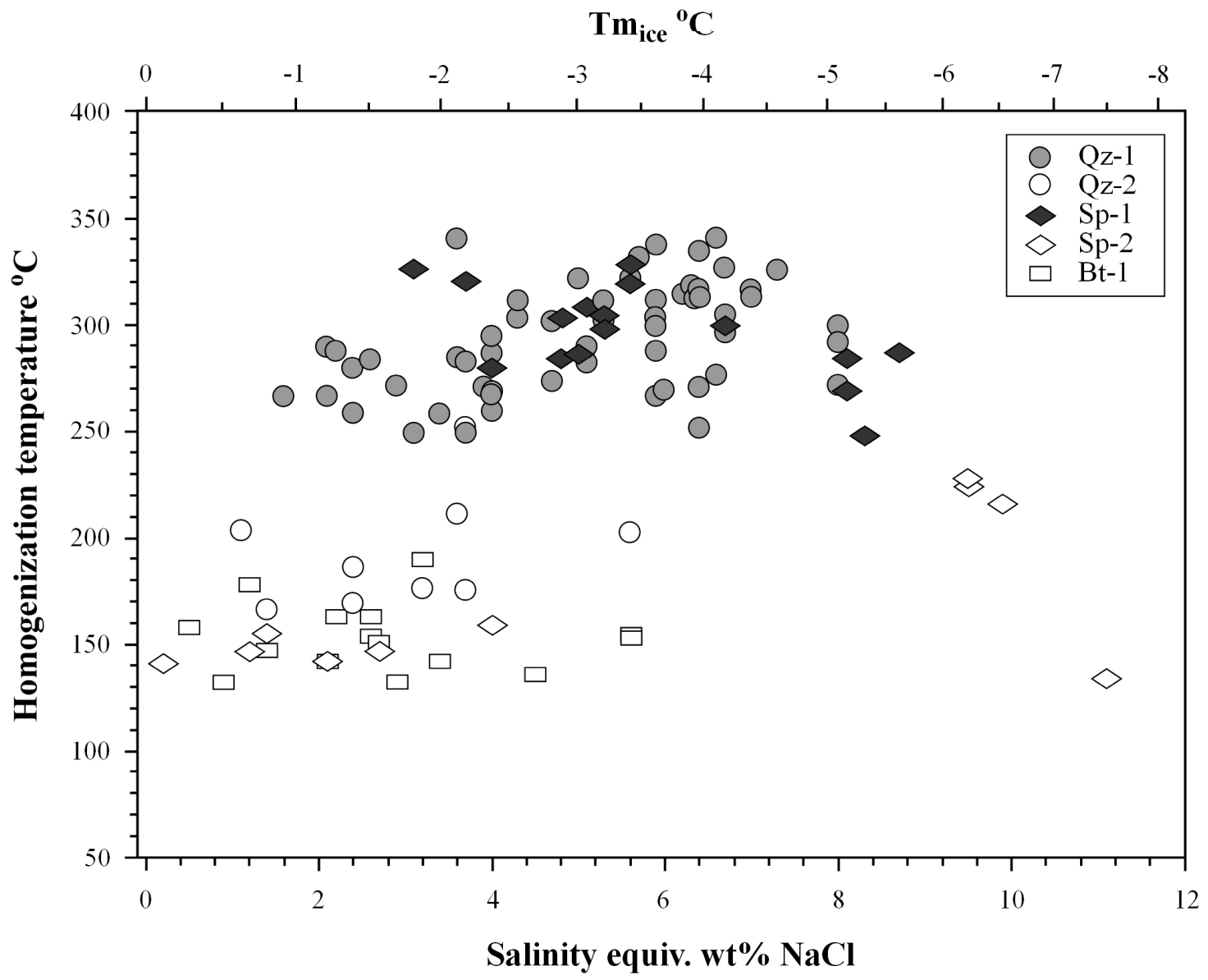


Figure 9-R2

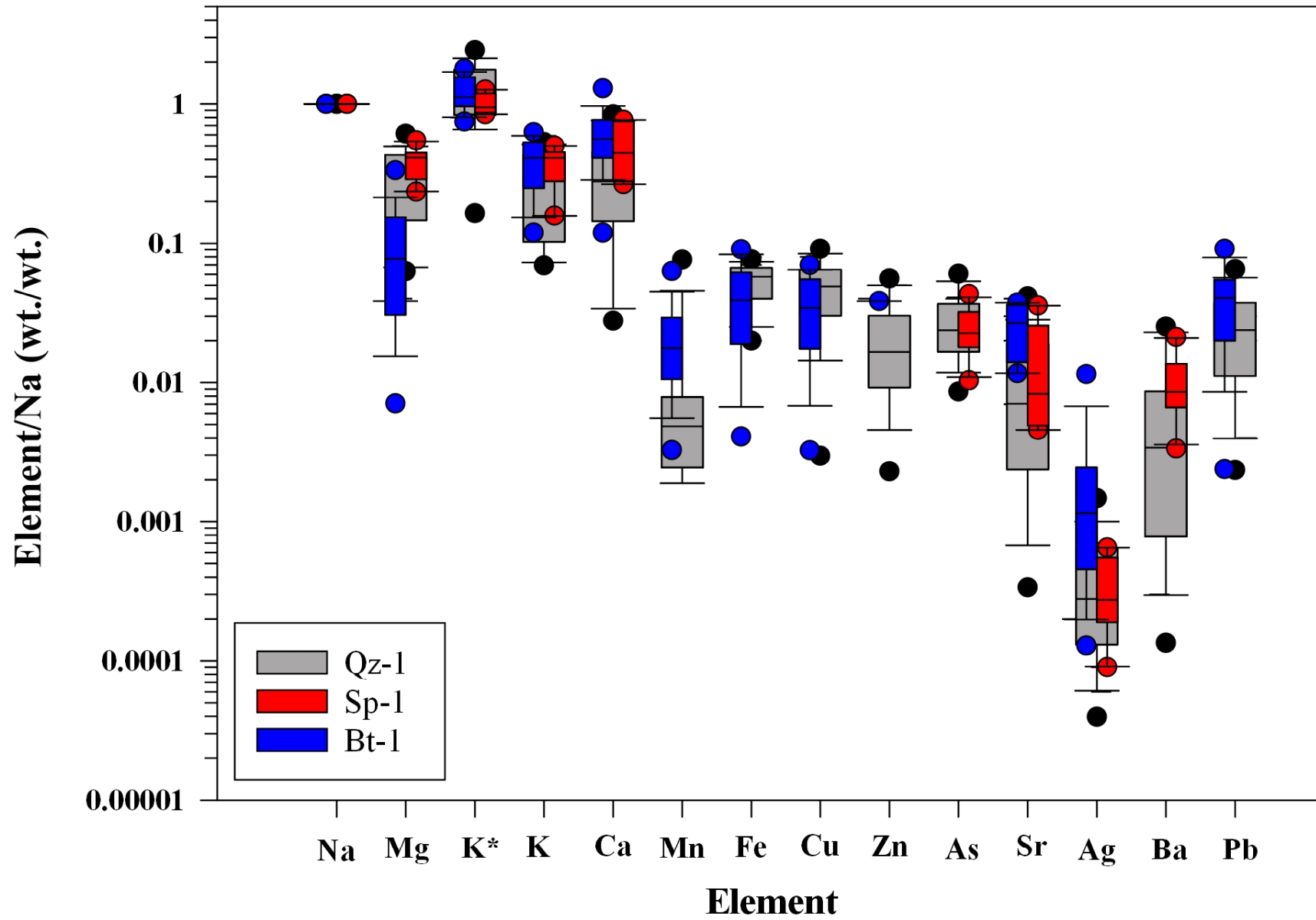


Fig. 10-R3

1  
2  
3  
4  
5  
6  
7  
8  
9  
10  
11  
12  
13  
14  
15  
16  
17  
18  
19  
20  
21  
22  
23  
24  
25  
26  
27  
28  
29  
30  
31  
32  
33  
34  
35  
36  
37  
38  
39  
40  
41  
42  
43  
44  
45  
46  
47  
48  
49  
50  
51  
52  
53  
54  
55

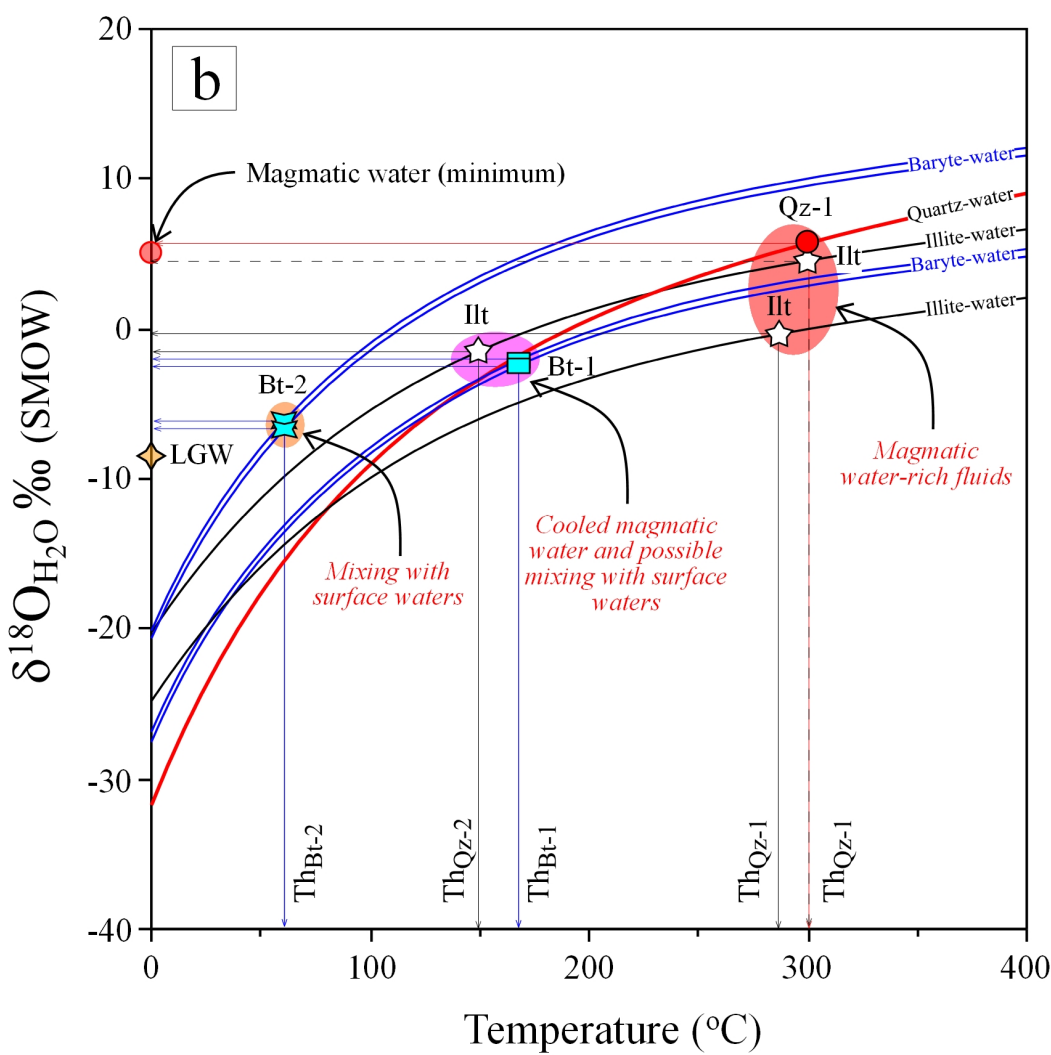
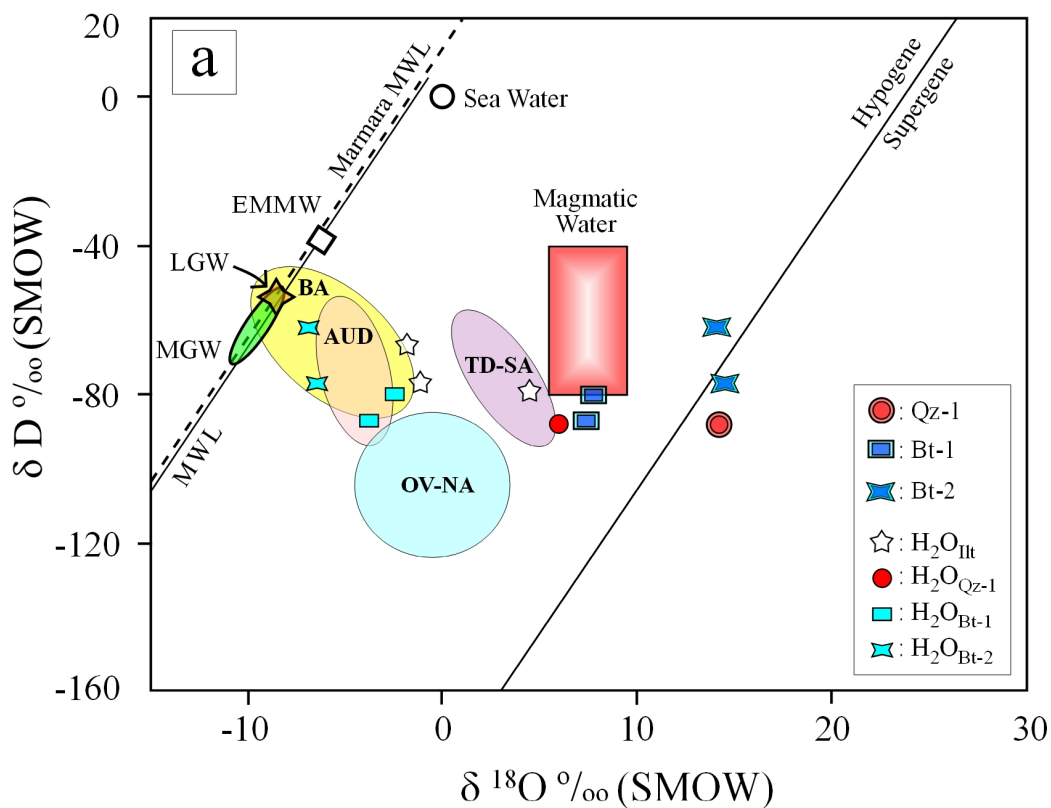


Figure 11-R2

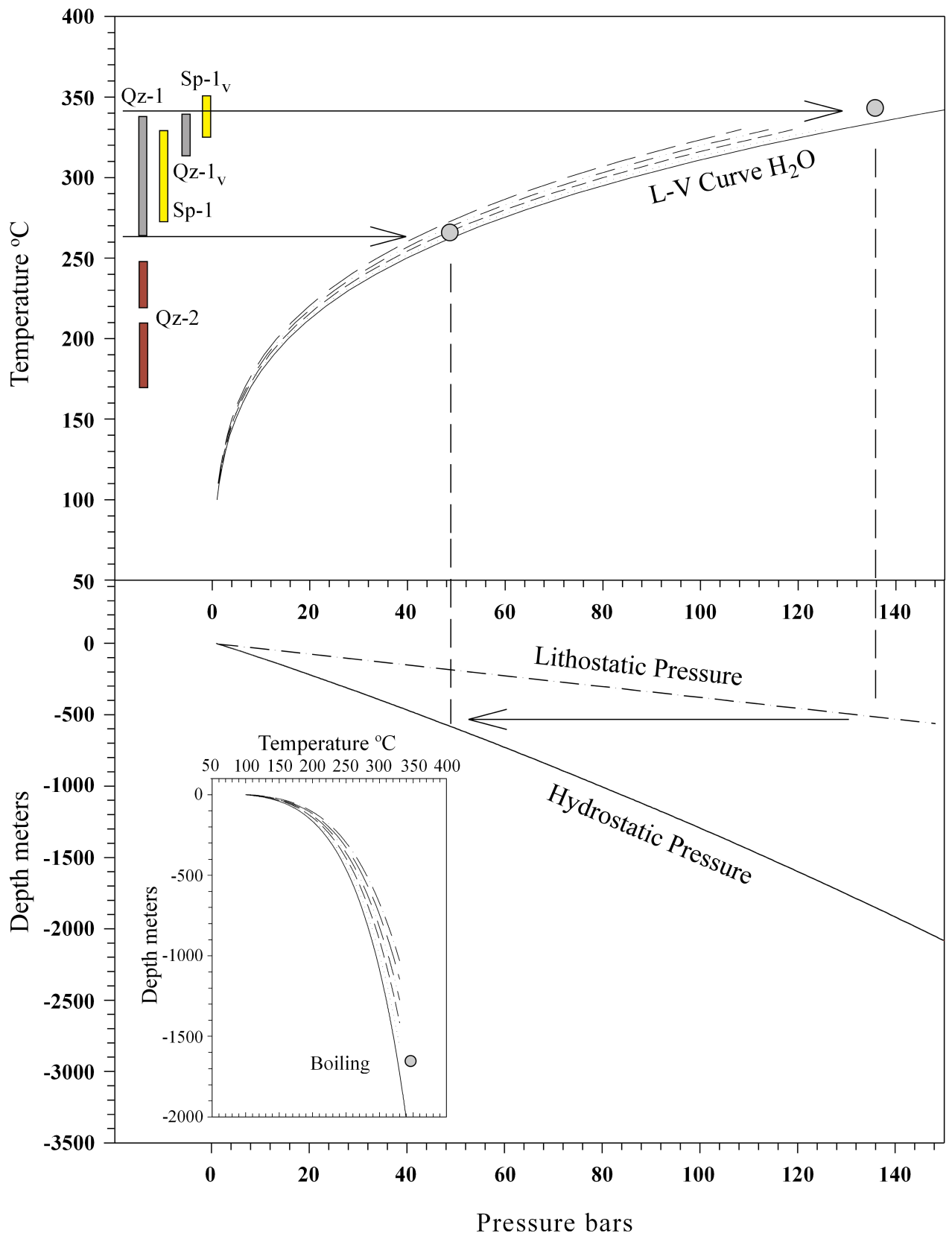


Figure 12-R2

**Table 1.** General characteristics of selected epithermal ore deposits in western and northwestern Turkey.

Deposit	Location	Deposit Style	Ore Mineral Assemblages(*)	Th °C	Salinity wt.%NaCl	$\delta^{18}\text{O}$ ‰	$\delta\text{D}$ ‰	References
Kisladag	Usak	Porphyry	Au, Gn, Sp, Mol	322-483	>35	None	None	Hanilci et al. 2015
Efemcukuru	Izmir	LS-IS	Au, Ag, Ccp, Py, Gn, Rds, Rdn	200-300	0-9	1.3 to 25.3	None	Oyman et al. 2003; Boucher, 2016
Kartaldag	Canakkale	HS	Py, Sp, Cv, Au	245-285	0-1.7	-7.95 to 1.49	None	Unal et al, 2013
Madendag	Canakkale	HS	Py, Sp, Au	235-255	0-0.7	-2.97 to 5.54	None	Unal et al, 2013
Tepeoba	Balikesir	Porphyry	Mo, Au, Py	500-600	>35	5 to 5.4	-69 to -61	Tufan et al, 2018
Soma	Balikesir	Porphyry	Ccp, Py, Au	250-400	20	None	None	Bozkaya et al, 2018
Arapucandere	Canakkale	LS-IS	Py, Ccp, Sp, Au	160-360	0-1.7	-8.5 to -1.7	-90 to -55	Bozkaya et al, 2008
Koru	Canakkale	IM-S	Gn, Sp, Py, Au	135-355	0.2-11	-13.5 to -6.4	-87 to -62	Bozkaya and Gökce, 2001
Tesbihdere/ Sahinli	Canakkale	IM-S	Gn, Sp, Py, Ccp, Au	170-360	0.5-10	None	None	Bozkaya et al, 2014
Balcilar	Canakkale	LS	Gn, Sp, Ccp, Py, Au	115-130	3.8-8.5	-0.23 to -6.95	-50	Bozkaya et al. 2011
Kuscayir	Canakkale	Porphyry HS	Mag, Ilm, Py, Apy, Ccp, Au	270-350 190-370	50 22.33-31.19	None	None	Yilmaz, 2003 Vural, 2006
Sindirgi	Balikesir	LS	Py, Au-Ag, Elc	157-330	0.5-4.8	None	None	Yilmaz et al, 2013
Ovacik	Balikesir	LS	Py, Ccp, Sp, Au, Apy	147-298	0-1.2	-2.9-3.5	-82 to -125	Yilmaz, 2002; Yilmaz et al, 2007
Kisacik	Canakkale	LS	Py, Au, Gth, Lm	190-320	0.16-6.5	None	None	Vural, 2006

(\*) Mineral abbreviations are taken from Whitney and Evans (2010). Au: Native gold, Ag: Native silver, Gn: Galena, Sp: Sphalerite, Py: Pyrite, Ccp: Chalcopyrite, Mol: Molybdenite, Rds: Rhodochrosite, Rdn: Rhodonite, Cv: Covellite, Apy: Arsenopyrite, Elc: Electrum, Mag: Magnetite, Gth: Goethite, Lm: Limonite

**Table 2.** Summary of the microthermometry data for inclusions from the Koru deposit.

Sample	Type	Mineralogy	Te °C	Tm ice °C			Salinity equiv. wt% NaCl			Th °C		
				Min	Max	Average	Min	Max	Average	Min	Max	Average
TK-20	L-V	Quartz-1	< -40	-3.2	-2.6	-3	4.3	5.1	4.9	289	325	309
	L-V	Quartz-2		-3.4	-2.1	-2.8	3.6	5.6	4.6	178	211	198
TK-21	L-V	Quartz-1	~-45	-5.1	-1.2	-3	2.1	8	5.0	249	329	287
	V	Quartz-1								315	342	331
	L-V	Quartz-2										3.2
TK-23	L-V	Quartz-1	~ -45	-5.1	-0.9	-2.8	1.6	8	4.6	258	316	290
	V	Quartz-1								329	340	332
	L-V	Quartz-2								-2.2	-0.6	-1.4
TK-29	L-V	Quartz-1	~ -50	-3.6	-2.8	-3.2	4.7	5.9	5.3	279	341	308
TK-34	L-V	Quartz-1	~ -40	-4.2	-1.5	-3.2	2.6	6.7	5.2	259	342	303
	L-V	Quartz-2										-2.2
	L-V	Sphalerite-1	~ -45	-5.6	-1.8	-3.6	3.1	8.7	5.8	248	331	296
	V	Quartz-1								328	354	343
TK-44	L-V	Baryte-2		-1.5	-1.3	-1.4	2.2	2.6	2.4	70	163	117
	L-V	Sphalerite-2		-6.5	-1.2	-4.4	2.1	9.9	6.7	142	228	191
TK-53	L-V	Quartz-1		-5.1	-2.1	-3.6	3.6	8	5.8	282	340	309
	L-V	Quartz-2				-8			1.4	166	211	186
TK-56	L-V	Baryte-1		-1.9	-0.7	-1.3	1.2	3.2	2.3	140	217	167
TK-61	L-V	Baryte-1		-3.4	-0.3	-1.8	0.5	5.6	3.0	113	192	143
	L-V	Sphalerite-2		-7.5	-0.1	-2.3	0.2	11.1	3.6	134	159	147
TK-83	L-V	Baryte-1		-3.4	-0.8	-1.9	1.4	5.6	3.2	140	217	167

**Table 3.** LA-ICP-MS analyses of individual fluid inclusions: Average element ratios (wt/wt relative to Na) and concentrations in ppm.

Sample	Salinity Wt% NaCl	Na	Mg	K*	K	Ca	Mn	Fe	Cu	Zn	As	Sr	Ag	Ba	Pb	
TK-20	Average	1	.337	<i>1.376</i>	.441	.481	.0052	.049	.044	.018	.030	.016	.001	.0067	.034	
Quartz	Std Dev		.201	<i>.588</i>	.09	.234	.003	.016	.022	.009	.017	.008	.0006	.002	.019	
	<b>4.9</b>	<b>ppm*</b>	<b>7980</b>	<b>2691</b>		<b>3516</b>	<b>3863</b>	<b>41</b>	<b>393</b>	<b>350</b>	<b>144</b>	<b>240</b>	<b>127</b>	<b>8.1</b>	<b>53.2</b>	<b>274</b>
TK-21	Average	1	.246	<i>1.094</i>	.250	.165	.0045	.059	.056	.0112	.032	.002	.002	.0009	.0165	
Quartz	Std Dev		.177	<i>.659</i>	.169	.122	.003	.018	.027	.007	.014	.002	.0002	.0008	.013	
	<b>5.0</b>	<b>ppm*</b>	<b>10668</b>	<b>2629</b>		<b>2665</b>	<b>1765</b>	<b>48</b>	<b>632</b>	<b>597</b>	<b>126</b>	<b>338</b>	<b>22</b>	<b>2.6</b>	<b>9.7</b>	<b>176</b>
TK-29	Average	1	.382	<i>1.08</i>	.230	.530	.059	.038	.020	.033	.022	.017	.0003	.0104	.013	
Quartz	Std Dev		.184	<i>.609</i>	.147	.243	.022	na	na	.019	.014	.013	.0002	.010	na	
	<b>5.3</b>	<b>ppm*</b>	<b>8338</b>	<b>3187</b>		<b>1921</b>	<b>4422</b>	<b>494</b>	<b>316</b>	<b>166</b>	<b>278</b>	<b>183</b>	<b>143</b>	<b>2.6</b>	<b>116</b>	<b>112</b>
TK-34	Average	1	.387	<i>1.011</i>	.369	.505					.025	.014	.00035	.010	.006	
Sphalerite	Std Dev		.099	<i>.175</i>	.116	.239					.009	.012	.00021			
	<b>5.8</b>	<b>ppm*</b>	<b>9743</b>	<b>3771</b>		<b>3592</b>					<b>239</b>	<b>137</b>	<b>3.4</b>	<b>101</b>		
TK-44	Average	1	.096				.031	.072	.039			.026	.0064		.048	
Baryte	Std Dev		.051				.020	.020	na			.011	.017		.013	
	<b>2.4</b>	<b>ppm*</b>														
TK-53	Average	1	.124	<i>1.609</i>	.464	.695	.031	.041								
Baryte	Std Dev		.121	<i>.283</i>	.127	.424	.025	.020								
	<b>3.0</b>	<b>ppm*</b>	<b>5013</b>	<b>621</b>		<b>2328</b>	<b>3486</b>	<b>158</b>	<b>204</b>							
TK-60	Average	1	.131	<i>1.274</i>	.310	.675	.035	.079	.049				.0062			
Baryte	Std Dev		.063	<i>.314</i>	.088	.273	.016	na	.016				.004			
	<b>3.0</b>	<b>ppm*</b>	<b>5168</b>	<b>675</b>		<b>1604</b>	<b>3489</b>	<b>179</b>	<b>410</b>	<b>253</b>			<b>32</b>			
TK-61	Average	1	.157	<i>1.217</i>	.278		.561	.020	.039	.025			.0008		.029	
Baryte	Std Dev		.121	<i>.365</i>	.168	.250	.014	.033	.022	na			.0006		.022	
	<b>3.0</b>	<b>ppm*</b>	<b>5498</b>	<b>862</b>		<b>1521</b>	<b>3087</b>	<b>113</b>	<b>215</b>	<b>139</b>	<b>211</b>		<b>4.2</b>		<b>161</b>	
TK-75	Average	1	.118	<i>1.117</i>	.479	.501	.019	.033	.042				.0028			
Baryte	Std Dev		.084	<i>.287</i>	.134	.205	.010	.021	.020				.0023			
	<b>3.0</b>	<b>ppm*</b>	<b>5381</b>	<b>638</b>		<b>2578</b>	<b>2694</b>	<b>100</b>	<b>180</b>	<b>224</b>			<b>15</b>			
TK-83	Average	1	.021	<i>1.160</i>	.439		.0145	.038	.039				.0007		.048	
Baryte	Std Dev		.014	<i>.308</i>	.146		.009	.022	.020				.0007		.023	
	<b>3.2</b>	<b>ppm*</b>														

(\*) Calculation of concentrations uses the lower values of K/Na. This is not affected by solid inclusions of illites which increase the K concentration (K\*/Na values). Where K/Na or Ca/Na ratios were not suitable, usually due to contamination by solid mineral phases, it was not possible to calculate ppm values for the other elements.

**Table 4.** Oxygen and hydrogen isotope data and calculated  $\delta^{18}\text{O}$  values for inclusion water in equilibrium with baryte and quartz from Koru samples. Data for quartz is taken from Bozkaya et al. (2016).

<b>Sample</b>	<b>Mineral</b>	<b><math>\delta \text{ D}</math> (‰)</b>	<b><math>\delta^{18}\text{O}</math> (‰)</b>	<b>Average Th (°C)</b>	<b><math>10^3 \ln \alpha</math></b>	<b>Calculated <math>\delta^{18}\text{O}</math> (‰)</b>
<b>TK-53-1</b>	Quartz	-88	14.2	300	8.2	6.0
<b>TK-61</b>	Baryte-I	-87	7.8	143	11.5	-3.7
<b>TK-75</b>	Baryte-I	n.d.	7.4	167	9.8	-2.4
<b>TK-83</b>	Baryte-I	-80	7.4	167	9.8	-2.4
<b>TK-44</b>	Baryte-II	-62	14.1	60	20.9	-6.8
<b>TK-56</b>	Baryte-II	-77	14.5	60	20.9	-6.4
<b>TK-60</b>	Baryte-II	n.d.	14.0	60	20.9	-6.9